Robust μ-optimal Control Synthesis for Modular Multiport DC-DC Converter

Farajdadian, Shahriar; Hajizadeh, Amin; Soltani, Mohsen; Bauer, Pavol; Vahedi, Hani

DOI
10.1109/ACCESS.2025.3610203

Publication date
2025

Document Version
Final published version

Published in
IEEE Access

IEEE Access
Multidisciplinary ⋮ Rapid Review ⋮ Open Access Journal

Received 19 August 2025, accepted 9 September 2025,
date of publication 16 September 2025, date of current version 25 September 2025.

Digital Object Identifier 10.1109/ACCESS.2025.3610203

RESEARCH ARTICLE

Robust μ−Optimal Control Synthesis for Modular Multi-Port DC-DC Converter

SHAHRIAR FARAJDADIAN[1,2], (Member, IEEE), AMIN HAJIZADEH[1], (Senior Member, IEEE), MOHSEN SOLTANI[1], (Senior Member, IEEE), PAVOL BAUER[2], (Senior Member, IEEE), AND HANI VAHEDI[2], (Senior Member, IEEE)

[1]AAU Energy, Aalborg University, 9220 Aalborg, Denmark
[2]Electrical Sustainable Energy Department, Delft University of Technology, 2628 CD Delft, The Netherlands

Corresponding author: Shahriar Farajdadian (Shfa@et.aau.dk)

ABSTRACT Owing to the intermittent characteristics of renewable energy sources (RESs) and the unpredictability of load demand, integrating multiple RESs and energy storage systems (ESSs) has become imperative. Modular Multi-port Converters (MMPC) have emerged as a viable solution to meet this need, offering superior performance, efficiency, and reliability compared to multiple SISO dc/dc converters. To this end, this paper presents a comprehensive model of an MMPC, which is bidirectional and capable of operating in both step-up and step-down modes. Following the derivation of the converter model, a robust μ−controller using the D−$\mathcal{G}-\mathcal{K}$ iterative procedure is designed. This controller addresses the cross-coupling challenges inherent in MIMO systems and effectively overcomes the parametric uncertainties associated with the converter. Finally, hardware-in-the-loop (HIL) test results derived from OPAL-RT 4610, and experimental results from a prototype are used to validate this control approach.

INDEX TERMS Dc/dc converter, multi-port converter, modular converter, robust control, μ−synthesis.

NOMENCLATURE

MPC	Multi-port DC/DC converter.
MMPC	Modular multi-port converter.
RES	Renewable energy source.
ESS	Energy storage system.
$MPDC^{SU}$	Step-up Multi-port DC/DC converter.
$MPDC^{SD}$	Step-down Multi-port DC/DC converter.
$MPDC^{SU}_{3L}$	3-level Step-up Multi-port DC/DC converter.
$MPDC^{SD}_{3L}$	3-level Step-down Multi-port DC/DC converter.
$MPDC^{SU}_{nL}$	n-level Step-up Multi-port DC/DC converter.
$MPDC^{SD}_{nL}$	n-level Step-up Multi-port DC/DC converter.
MIMO	Multi-input multi-output.
$V_{[n]}$	Voltage of port n.
$i_{[n]}$	Current of port n.
$i_{L[k,j]}$	Inductor current at row K, column j.
$d_{[K,j]}$	Duty cycle of a switch at row K, column j.
$v_{C[k,j]}$	Capacitor voltage at row K, column j.
μ_{Δ}	Structured singular values.
$\rho(\mathcal{M})$	Spectral radius of $\mathcal{M}$.
$\bar{\sigma}$	Maximum singular values.
SSV	Structure singular values.
$\mathbb{C}^{n\times m}$	Complex matrix with n rows and m columns.
$\mathcal{W}$	Exogenous inputs.
$\mathcal{Z}$	Exogenous outputs.
$\mathcal{P}$	Generalized plant.
$\mathcal{LLFT}$	Lower linear fractional transformation.
Sup	Supremum.
KcR	Reduced order controller.
HIL	Hardware-in-the-Loop.

The associate editor coordinating the review of this manuscript and approving it for publication was Ujjwol Tamrakar.

I. INTRODUCTION

Given the sporadic characteristics of RESs and the unpredictable nature of load demand, integrating multiple RESs and ESSs has become essential for mitigating output power

fluctuations and enhancing the reliability, stability, and cost-effectiveness of energy conversion systems. In this context, DC/DC converters play a crucial role in managing different energy sources, as well as stabilizing DC buses. In the literature, two approaches have been explored for integrating RESs and ESSs and interfacing them with loads/grids. The multi-converter approach involves employing individual single-input single-output (SISO) DC/DC converters for each RES and ESS, with their outputs interconnected through a shared DC-link. While this approach offers straightforward architecture, it suffers from high overall cost, low efficiency, and low power density. Moreover, the necessity for energy management, control, and communication among individual converters contributes to the complexity of such systems [1], [2], [3].

To address the abovementioned issues, MPCs have been suggested as a solution. MPCs can be broadly classified into two categories: isolated and non-isolated configurations. Isolated MPCs are commonly employed in medium and high power/voltage applications where galvanic isolation is required. However, transformer-based MPCs typically involve a higher component count and incorporate multiple high-frequency or multi-winding transformers, thereby increasing the overall size. Consequently, this approach can be costly and may lead to lower power density and reliability [4], [5]. On the contrary, non-isolated topologies are highly efficient and cost-effective with a lower component count; however, they often suffer from lower voltage gain. To alleviate voltage gain drawback, methods such as switched capacitors [6], coupled inductors [7], [8], and voltage multipliers are recommended in the literature.

Another approach to address the voltage gain limitation in higher- power/voltage applications is to employ expandable modular topologies. MMPCs with standard submodules, not only help reduce voltage stress on the switches but also enhance the overall reliability and flexibility of the power conversion system [9], [10], [11], [12], [13]. Several MMPCs have been proposed and discussed in the literatures [14], [15], [16], [17], [18], [19], [20], and [21]. A fully modular MPC is proposed in [15]. This MMPC comprises identical converter modules that can be connected in parallel and/or series, offering scalability and flexibility. Such a structure is well-suited for applications requiring high power handling capability and large voltage conversion ratios. Furthermore, the suggested topology supports bidirectional power flow, allowing for energy exchange at intermediate voltage nodes and facilitating both step-up and step-down operations. The soft-switching operation of the converter is addressed in [16] and [17], where an auxiliary Zero-Current Transition (ZCT) cell is introduced to enable zero-current turn-on and turn-off for all switches. This auxiliary cell consists of two additional switches, a resonant inductor, and a resonant capacitor. A distributed control of the MMPC consisting of a central controller and localized controllers is described in [16]. In [14], an expandable MMPC comprised of the voltage multiplier cell with high voltage gain is proposed. However, the charging path is not provided for the ESS from other input ports.

MPC presents several challenges in the context of controller design. [2]. These complexities stem from the inherent cross-coupling of power flows among input-output ports, which significantly influences the design, stability, performance, and robustness of the control system [22], [23], [24], [25]. Various decentralized PID controller design approaches are explored in the literature for MIMO systems [26], [27], [28]. However, achieving global stability and desirable performance while effectively mitigating interaction effects remains a challenge [29], [30]. Consequently, a centralized approach is often preferred. The conventional approach for designing a control system for MPCs involves utilizing decoupling networks. In this method, a state-space model of the MPC is obtained, and subsequently, a decoupling network is introduced to enable separate controller designs [31], [32], [33], [34]. However, as the number of input/output ports (or modules) of the MPC (MMPC) increases, the complexity of designing the decoupling network increases, which may require model reduction [35], [36]. Reference [37] employs a software decoupling strategy integrating PID control, model predictive control, and fuzzy compensation to mitigate cross-coupling effects. While effective, the approach's substantial computational requirements may constrain real-time operation and increase implementation expenses. In [38]a software-based feedback linearization controller effectively suppressed cross-coupling, but improper non-linear inversion could degrade performance. In addition, RHP zeroes can further restrict the decoupling network design [36].

One important yet often-overlooked aspect in designing controllers for MPCs is the robust stability and performance considerations in the presence of various uncertainties. Considerable research has been devoted to robust controller design using the loop-shaping method in SISO systems. However, unlike SISO systems, shaping the open-loop and tuning the controller parameters to achieve the desired performance and robustness is considerably more challenging in MIMO systems [39]. In addition, most research studies have primarily focused on uncertainties in input sources or loads, often neglecting parameter uncertainties within the converter itself. For a double-input double-output (DIDO) converter H_∞−loop shaping controller is discussed in [40]. However, [40] adopted a decoupling approach and only accounted for uncertainties in input voltage sources and loads, neglecting uncertainties in converter parameters. In [35], a centralized robust LMI-based controller using D-stability pole placement is discussed for a double-input single-output (DISO) isolated converter. However, [35]does not consider parametric uncertainties. A Lyapunov-based controller for an SIDO converter is discussed in [41]. In [42]an LMI-based H_∞ controller is designed for a DISO DC/DC converter for a charge-pump application. Appendix A presents a

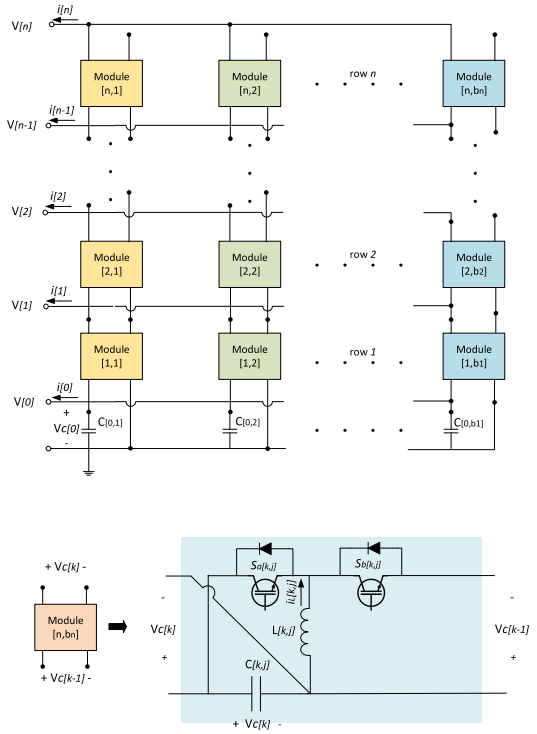

FIGURE 1. Topology of MMPC.

comparative overview of several robust control techniques from multiple perspectives.

The primary contribution of this research is the development of a robust controller for a bidirectional modular multi-port converter(MMPC) capable of operating in both step-up and step-down modes. The robust controller is synthesized not only to address the cross-coupling challenges inherent in MPCs and effectively manage the parametric uncertainties of MMPCs but also to achieve a less conservative and lower-order controller design. To achieve this, following the derivation of the converter model in both step-up and step-down modes, a centralized controller is synthesized using the robust $\mu-$optimal approach through the $D-\mathcal{G}-\mathcal{K}$ iterative procedure.

The rest of the paper is organized as follows: In section II, generalized non-linear dynamic equations of the non-isolated $MPDC_{nL}^{SU}$ and $MPDC_{nL}^{SD}$ are obtained. Subsequently, non-linear dynamic equations and small-signal dynamic equations for $MPDC_{3L}^{SU}$ and $MPDC_{3L}^{SD}$, along with the corresponding state-space model, are obtained. Section III discusses the necessary and sufficient conditions for robust stability and performance of MIMO-systems and explains the $D-\mathcal{G}-\mathcal{K}$ algorithm. Section IV presents HIL test results derived from OPAL-RT 4610 and experimental results from a prototype used to validate the control strategy. Finally, section V is the concluding remarks.

II. EXPANDABLE BIDIRECTIONAL MMPC

A. CONVERTER TOPOLOGY

Fig.1 illustrates the configuration of the non-isolated MMPC converter [15]. The converter features a fully modular architecture, composed of identical converter modules that can be connected in parallel and/or series. This modular design facilitates scalability, making it well-suited for high-power and high-conversion-ratio applications. Moreover, the converter supports bidirectional power flow, which is essential for interfacing with ESSs such as batteries and supercapacitors, as it enables both charging (energy absorption) and discharging (energy delivery) modes. In this configuration, n signifies the number of modules connected in series, and b_k represents the number of parallel modules in the row k. The controllable voltage ports, denoted as $V_{[0]},\ldots,\ V_{[n]}$, have the flexibility to serve as input, output, or energy storage ports. Theoretically, this design allows for the extension of the converter to accommodate any desired voltage levels. While the modules of the MMPC are based on buck-boost converter topologies, they are not limited to this topology, and other converter types that conform to the overall system configuration may also be employed. Switches $S_{a[K,j]}$ and $S_{b[k,j]}$ in each module operate complementarily, and for applications requiring bidirectional power flow, antiparallel diodes are necessary. In $n-$level non-isolated MMPC, one of the nodes must be designated as a reference node (slack node) to ensure internal power balance within the converter. The reference node is typically modeled as a voltage source v_i with an unregulated current, meaning it adjusts its current output as needed to maintain voltage levels. Depending on the application, the selection of the reference node is left to the discretion of the designer. The choice of reference node directly influences the resulting converter configuration, leading to different circuit topologies. In this study, two such configurations are investigated: $MPDC_{nL}^{SD}$ and $MPDC_{nL}^{SU}$.

B. OPERATING PRINCIPLE OF THE PROPOSED CONVERTER

The dynamic equations of the $MPDC_{nL}^{SD}$ can be expressed using (1) and (2), respectively. In these equations, the source v_i is connected to the port $V_{[n]}$, and $v_{C[k]}$ and $i_{L[k]}$ indicate the capacitor voltage and inductor current in the k_{th} row, respectively. Additionally, $V_{[k]}$ denotes the voltage from the k_{th} port to ground, and R_L represents the internal resistances of the inductors.

$$
\begin{aligned}
&L\frac{di_{L[k,j]}}{dt}\\
&=\begin{cases}
v_{C[k-1]}d_{[K,j]}-v_{C[k]}\left(1-d_{[K,j]}\right)-i_{L[k,j]}R_L,\\
\qquad k=1,\ \forall j\in\{1,\ldots,b_k\}\\
v_{C[k-1]}d_{[K,j]}-\left(v_i-\sum_{h=0}^{n-1}v_{C[h]}\right)\left(1-d_{[K,j]}\right)\\
-i_{L[k,j]}R_L,\\
\qquad k=n,\forall j\in\{1,\ldots,b_k\}
\end{cases}
\end{aligned}
\tag{1}
$$

$$
b_kC\frac{dv_{C[k]}}{dt}
$$

$$= \begin{cases} -\sum_{j=1}^{b_{k+1}} i_{L[k+1,j]} + \sum_{j=1}^{b_{k+2}} i_{L[k+2,j]} \left(d_{[K+2,j]}\right) + b_{k+1} C \frac{dv_{C[k+1]}}{dt} - i_{[k]}, \\ k = 0 \\ \sum_{j=1}^{b_k} i_{L[k,j]} \left(1 - d_{[K,j]}\right) - \sum_{j=1}^{b_{k+1}} i_{L[k,j]} \\ + \sum_{j=1}^{b_{k+2}} i_{L[k+2,j]} \left(d_{[K+2,j]}\right) \\ + b_{k+1} C \frac{dv_{C[k+1]}}{dt} - i_{[k]}, \qquad k \in \{1, \ldots, n-1\} \\ \sum_{j=1}^{b_k} i_{L[k,j]} \left(1 - d_{[K,j]}\right) - i_{[k]} - \sum_{j=1}^{b_{k+1}} i_{L[k+1,j]} \\ + b_{k+1} C \left(\frac{dv_i}{dt} - \sum_{h=0}^{n-1} \frac{dv_{C[h]}}{dt}\right), \; k = n-1 \end{cases} \tag{2}$$

For controller synthesis simplicity, (2) can be rearranged to the form of (3), as shown at the bottom of the page:

The matrix $[H]$ is defined as (4):

$$[H] = \begin{bmatrix} 1 & -1 & \cdots & 0 & 0 \\ 0 & 1 & \ldots & 0 & 0 \\ \vdots & \vdots & \ddots & \vdots & \vdots \\ 0 & 0 & \cdots & 1 & -1 \\ \frac{b_n}{b_1} & \frac{b_n}{b_1} & \cdots & \frac{b_n}{b_{n-2}} & \frac{b_{n-1}+b_n}{b_{n-1}} \end{bmatrix} \tag{4}$$

Similarly, the dynamic equations of the $MPDC_{nL}^{SU}$ can be expressed using (5) and (6), respectively, whereas the source v_i is connected to the port $V_{[0]}$.

$$b_k C \frac{dv_{C[k]}}{dt} = \begin{cases} \sum_{j=1}^{b_k} i_{L[k,j]}(1 - d_{[K,j]})) - \sum_{j=1}^{b_{k+1}} i_{L[k+1,j]} \left(d_{[K+1,j]}\right) \\ -\sum_{h=k}^{n} i_{[h]}, \quad k \in \{1, \ldots, n-1\} \\ \sum_{j=1}^{b_k} i_{L[k,j]} \left(1 - d_{[K,j]}\right) - i_{[k]}, \quad k = n \end{cases} \tag{5}$$

$$L \frac{di_{L[k,j]}}{dt} = \begin{cases} v_i d_{[K,j]} - v_{C[k]} \left(1 - d_{[K,j]}\right) - i_{L[k,j]} R_L, \\ k = 1, \; \forall j \in \{1, \ldots, b_k\} \\ v_{C[k-1]} d_{[K,j]} - v_{C[k]} \left(1 - d_{[K,j]}\right) - i_{L[k,j]} R_L, \\ k = n \end{cases} \tag{6}$$

Similar to (3) and (4), (5) can be rearranged to the form of (7), as shown at the bottom of the page, where the matrix $[R]$ is defined as (8), as shown at the bottom of the page.

C. LINEAR EQUATIONS FOR MMPC

Configuration of $MPDC_{3L}^{SU}$ is shown in Fig.2.As can be seen, the voltage source v_i is connected to $v_{[0]}$, the current source $I_{s[1]}$ is linked to $v_{[1]}$, and loads R_2 and R_3 are connected to $v_{[2]}$ and $v_{[3]}$, respectively. From (5) and (6), the dynamic equations for the capacitor voltages and inductor currents can

$$[H] \begin{bmatrix} \\ b_1 C \frac{dv_{C[0]}}{dt} \\ b_1 C \frac{dv_{C[1]}}{dt} \\ . \\ . \\ . \\ b_{n-2} C \frac{dv_{C[n-2]}}{dt} \\ b_{n-1} C \frac{dv_{C[n-1]}}{dt} \end{bmatrix} = \begin{bmatrix} -\sum_{j=1}^{b_1} i_{L[1,j]} + \sum_{j=1}^{b_2} (i_{L[2,j]} d_{[2,j]}) - i_{[0]} \\ \sum_{j=1}^{b_1} \left(i_{L[1,j]} \left(1 - d_{[1,j]}\right)\right) - \sum_{j=1}^{b_2} i_{L[2,j]} + \sum_{j=1}^{b_3} \left(i_{L[3,j]} d_{[3,j]}\right) - i_{[1]} \\ . \\ . \\ . \\ \sum_{j=1}^{b_{n-2}} \left(i_{L[n-2,j]} \left(1 - d_{[n-2,j]}\right)\right) - \sum_{j=1}^{b_{n-1}} i_{L[n-1,j]} + \sum_{j=1}^{b_n} \left(i_{L[n,j]} d_{[n,j]}\right) \\ -i_{[n-2]} \\ \sum_{j=1}^{b_{n-1}} \left(i_{L[n-1,j]} \left(1 - d_{[n-1,j]}\right)\right) - \sum_{j=1}^{b_n} i_{L[n,j]} + b_n C \frac{dv_i}{dt} - i_{[n-1]} \end{bmatrix} \tag{3}$$

$$\begin{bmatrix} C \frac{dv_{C[1]}}{dt} \\ . \\ . \\ . \\ C \frac{dv_{C[n-1]}}{dt} \\ C \frac{dv_{C[n]}}{dt} \end{bmatrix} = [R] \times \begin{bmatrix} \sum_{j=1}^{b_1} i_{L[1,j]} \left(1 - d_{[1,j]}\right) - \sum_{j=1}^{b_2} i_{L[2,j]} \left(d_{[2,j]}\right) - \sum_{h=1}^{n} i_{[h]} \\ . \\ . \\ . \\ \sum_{j=1}^{b_{n-1}} i_{L[n-1,j]}(1 - d_{[n-1,j]})) - \sum_{j=1}^{b_n} i_{L[n,j]} \left(d_{[n,j]}\right) - \sum_{h=n-1}^{n} i_{[h]} \\ \sum_{j=1}^{b_n} i_{L[n,j]} \left(1 - d_{[n,j]}\right) - i_{[n]} \end{bmatrix} \tag{7}$$

$$[R] = \begin{bmatrix} \frac{1}{b_1} & \cdots & 0 \\ \vdots & \ddots & \vdots \\ 0 & \cdots & \frac{1}{b_n} \end{bmatrix} \tag{8}$$

be presented as (9) and (10).

$$\begin{cases} C\dfrac{dv_{C[1]}}{dt} = i_{L[1]}\left(1-d_{[1]}\right) - i_{L[2]}\left(d_{[2]}\right) - i_{[1]} - i_{[2]} - i_{[3]} \\ C\dfrac{dv_{C[2]}}{dt} = i_{L[2]}\left(1-d_{[2]}\right) - i_{L[3]}\left(d_{[3]}\right) - i_{[2]} - i_{[3]} \\ C\dfrac{dv_{C[3]}}{dt} = i_{L[3]}\left(1-d_{[3]}\right) - i_{[3]} \end{cases} \tag{9}$$

$$\begin{cases} L\dfrac{di_{L[1]}}{dt} = v_i d_{[1]} - v_{C[1]}\left(1-d_{[1]}\right) \\ L\dfrac{di_{L[2]}}{dt} = v_{C[1]} d_{[2]} - v_{C[2]}\left(1-d_{[2]}\right) \\ L\dfrac{di_{L[3]}}{dt} = v_{C[3]} d_{[3]} - v_{C[3]}\left(1-d_{[3]}\right) \end{cases} \tag{10}$$

By employing (9) and (10), the small-signal equations for capacitor voltages and inductor currents can be derived subsequently:

$$\begin{cases} C\dfrac{d\tilde{v}_{c[1]}}{dt} = \tilde{\imath}_{L[1]} - \tilde{\imath}_{L[1]}D_{[1]} - I_{L[1]}\tilde{d}_{[1]} - I_{L[2]}\tilde{d}_{[2]} \\ -\tilde{\imath}_{L[2]}D_{[2]} \\ -\tilde{\imath}_{[1]} - \tilde{\imath}_{[2]} - \tilde{\imath}_{[3]} \\ C\dfrac{d\tilde{v}_{c[2]}}{dt} = \tilde{\imath}_{L[2]} - \tilde{\imath}_{L[2]}D_{[2]} - I_{L[2]}\tilde{d}_{[2]} - I_{L[3]}\tilde{d}_{[3]} \\ -\tilde{\imath}_{L[3]}D_{[3]} \\ -\tilde{\imath}_{[2]} - \tilde{\imath}_{[3]} \\ C\dfrac{d\tilde{v}_{c[3]}}{dt} = \tilde{\imath}_{L[3]} - \tilde{\imath}_{L[3]}D_{[3]} - I_{L[3]}\tilde{d}_{[3]} - \tilde{\imath}_{[3]} \end{cases} \tag{11}$$

$$\begin{cases} L\dfrac{d\tilde{\imath}_{L[1]}}{dt} = v_i\tilde{d}_{[1]} + D_{[1]}\tilde{v}_i + v_{C[1]}\tilde{d}_{[1]} - \tilde{v}_{c[1]} + \tilde{v}_{c[1]}D_{[1]} \\ L\dfrac{d\tilde{\imath}_{L[2]}}{dt} = v_{C[1]}\tilde{d}_{[2]} + D_{[2]}\tilde{v}_{c[1]} + v_{C[2]}\tilde{d}_{[2]} - \tilde{v}_{c[2]} \\ +\tilde{v}_{c[2]}D_{[2]} \\ L\dfrac{d\tilde{\imath}_{L[3]}}{dt} = v_{C[2]}\tilde{d}_{[3]} + D_{[3]}\tilde{v}_{c[2]} + v_{C[3]}\tilde{d}_{[3]} - \tilde{v}_{c[3]} \\ +\tilde{v}_{c[3]}D_{[3]} \end{cases} \tag{12}$$

Equations (11) and (12) can be represented in state space form as (13)-(16). In this context, the state vector, x, the disturbance vector Γ, and the control vector u, are defined as given in (14).

$$\begin{cases} X = Ax + Bu + E\Gamma \\ Y = Cx + Du + G\Upsilon \end{cases} \tag{13}$$

$$\begin{cases} x = \left[v_{C[1]}, v_{C[2]}, v_{C[3]},\ i_{L[1]}, i_{L[2]}, i_{L[3]}\right]^T \\ u = \left[d_{[1]}, d_{[2]}, d_{[3]}\right]^T,\ \Gamma = \left[v_i, i_{[1]}, i_{[2]}, i_{[3]}\right]^T \end{cases} \tag{14}$$

$$A = \begin{bmatrix} 0 & 0 & 0 & \frac{1-d_1}{C} & \frac{-d_2}{C} & 0 \\ 0 & 0 & 0 & 0 & \frac{1-d_2}{C} & \frac{-d_3}{C} \\ 0 & 0 & 0 & 0 & 0 & \frac{1-d_3}{C} \\ \frac{d_1-1}{L} & 0 & 0 & 0 & 0 & 0 \\ \frac{d_2}{L} & \frac{d_2-1}{L} & 0 & 0 & 0 & 0 \\ 0 & \frac{d_3}{L} & \frac{d_3-1}{L} & 0 & 0 & 0 \end{bmatrix} \tag{15}$$

$$B = \begin{bmatrix} \frac{\tilde{\imath}_{L[1]}}{C} & \frac{\tilde{\imath}_{L[2]}}{C} & 0 \\ 0 & \frac{\tilde{\imath}_{L[2]}}{C} & \frac{\tilde{\imath}_{L[3]}}{C} \\ 0 & 0 & \frac{\tilde{\imath}_{L[3]}}{C} \\ \frac{v_i+v_{C[1]}}{L} & 0 & 0 \\ 0 & \frac{v_{C[1]}+v_{C[2]}}{L} & 0 \\ 0 & 0 & \frac{v_{C[2]}+v_{C[3]}}{L} \end{bmatrix},$$

$$E = \begin{bmatrix} 0 & \frac{-1}{C} & \frac{-1}{C} & \frac{-1}{C} \\ 0 & 0 & \frac{-1}{C} & \frac{-1}{C} \\ 0 & 0 & 0 & \frac{-1}{C} \\ \frac{d_1}{L} & 0 & 0 & 0 \\ 0 & 0 & 0 & 0 \\ 0 & 0 & 0 & 0 \end{bmatrix} \tag{16}$$

Configuration of $MPDC_{3L}^{SD}$ is shown in Fig. 3. As can be seen, the voltage source v_i is connected to $v_{[3]}$, current source $I_{s[1]}$ is linked to $v_{[1]}$, and loads R_2 and R_0 are connected to $v_{[2]}$ and $v_{[0]}$, respectively. From (1) and (2), the dynamic equations for the capacitor voltages and inductor currents can be presented as (17) and (18). It should be noted that $v_{C[3]}$ and $\frac{dv_{C[3]}}{dt}$ in (18) can be computed from (19).

$$\begin{cases} \dfrac{dv_{C[0]}}{dt} = -i_{L[1]} + i_{L[2]}\left(d_{[2]}\right) - i_{[1]} + C\dfrac{dv_{C[1]}}{dt} - i_{[0]} \\ \dfrac{dv_{C[1]}}{dt} = i_{L[1]}\left(1-d_{[1]}\right) - i_{L[2]} + i_{L[3]}\left(d_{[3]}\right) \\ +C\dfrac{dv_{C[2]}}{dt} - i_{[1]} \\ \dfrac{dv_{C[2]}}{dt} = i_{L[2]}\left(1-d_{[2]}\right) - i_{L[3]} + C\dfrac{dv_{C[3]}}{dt} - i_{[2]} \end{cases} \tag{17}$$

$$\begin{cases} L\dfrac{di_{L[1]}}{dt} = v_{C[0]}d_{[1]} - v_{C[1]}\left(1-d_{[1]}\right) \\ L\dfrac{di_{L[2]}}{dt} = v_{C[1]}d_{[2]} - v_{C[2]}\left(1-d_{[2]}\right) \\ L\dfrac{di_{L[3]}}{dt} = v_{C[2]}d_{[3]} - v_{C[3]}\left(1-d_{[3]}\right) \end{cases} \tag{18}$$

$$\begin{cases} v_{C[3]} = v_i - \sum_{j=0}^{2} v_{C[j]} \\ \dfrac{dv_{C[3]}}{dt} = \dfrac{dv_i}{dt} - \sum_{j=0}^{2} \dfrac{dv_{C[j]}}{dt} \end{cases} \tag{19}$$

The state-space realization of the average small-signal equations for the $MPDC_{3L}^{SD}$ can be derived from (20)-(22). In this context, the state vector, x, the disturbance vector Γ,and the control vector u, are defined as given in (20). It should be emphasized that $v_{C[3]}$ and $\frac{dv_{C[3]}}{dt}$ can be derived from (19), and hence $v_{C[3]}$ is not regarded as an independent state variable

$$\begin{cases} x = \left[v_{C[0]}, v_{C[1]}, v_{C[2]},\ i_{L[1]}, i_{L[2]}, i_{L[3]}\right]^T \\ u = \left[d_{[1]}, d_{[2]}, d_{[3]}\right]^T,\ \Gamma = \left[v_i, \dot{v}_i, i_{[1]}, i_{[2]}, i_{[3]}\right]^T \end{cases} \tag{20}$$

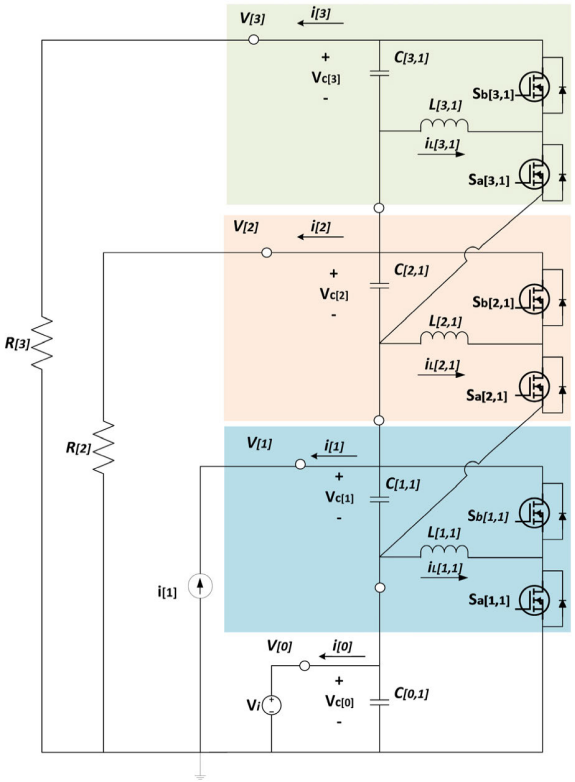

FIGURE 2. Configuration of $MPDC_{3L}^{SU}$.

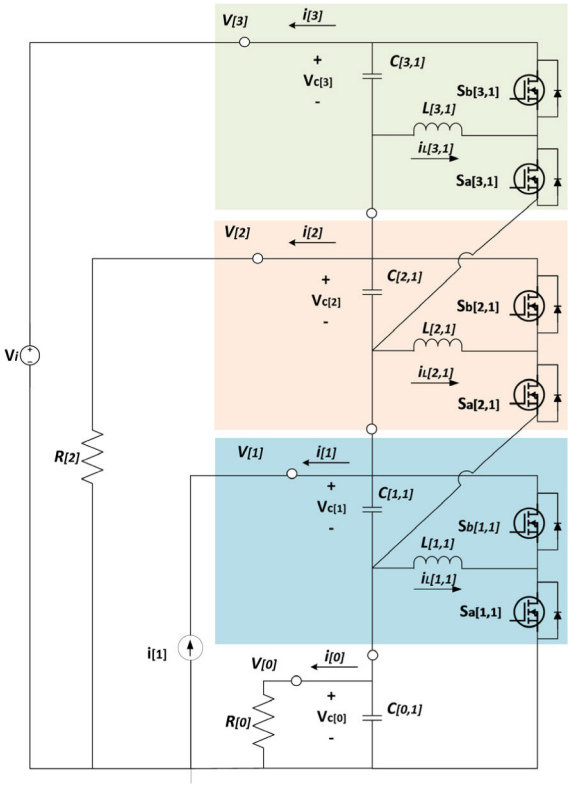

FIGURE 3. Configuration of $MPDC_{3L}^{SD}$.

$$A = \begin{bmatrix} 0 & 0 & 0 & \frac{-\left(\frac{d_1}{2}+\frac{1}{4}\right)}{C} & \frac{\left(\frac{d_2}{2}-\frac{1}{4}\right)}{C} & \frac{\left(\frac{d_3}{2}-\frac{1}{4}\right)}{C} \\ 0 & 0 & 0 & \frac{-\left(\frac{d_1}{2}-\frac{3}{4}\right)}{C} & \frac{-\left(\frac{d_2}{2}+\frac{1}{4}\right)}{C} & \frac{\left(\frac{d_3}{2}-\frac{1}{4}\right)}{C} \\ 0 & 0 & 0 & \frac{\left(\frac{d_1}{2}-\frac{1}{4}\right)}{C} & \frac{-\left(\frac{d_2}{2}-\frac{3}{4}\right)}{C} & \frac{-\left(\frac{d_3}{2}+\frac{1}{4}\right)}{C} \\ \frac{d_1}{L} & \frac{d_1-1}{L} & 0 & 0 & 0 & 0 \\ 0 & \frac{d_2}{L} & \frac{d_2-1}{L} & 0 & 0 & 0 \\ \frac{1-d_3}{L} & \frac{1-d_3}{L} & \frac{1}{L} & 0 & 0 & 0 \end{bmatrix} \tag{21}$$

$$B = \begin{bmatrix} \frac{-i_{L[1]}}{2C} & \frac{i_{L[2]}}{2C} & \frac{i_{L[3]}}{2C} \\ \frac{-i_{L[1]}}{2C} & \frac{-i_{L[2]}}{2C} & \frac{i_{L[3]}}{2C} \\ \frac{i_{L[1]}}{2C} & \frac{-i_{L[2]}}{2C} & \frac{-i_{L[3]}}{2C} \\ \frac{v_{C[1]}+v_{C[2]}}{L} & 0 & 0 \\ 0 & \frac{v_{C[2]}+v_{C[3]}}{L} & 0 \\ 0 & 0 & \frac{-\left(v_{C[1]}+v_{C[2]}-v_i\right)}{L} \end{bmatrix} \tag{22}$$

$$E = \begin{bmatrix} 0 & \frac{1}{4} & \frac{-3}{4C} & \frac{-1}{2C} & \frac{-1}{4C} \\ 0 & \frac{1}{4} & \frac{1}{4C} & \frac{-1}{2C} & \frac{-1}{4C} \\ 0 & \frac{1}{4} & \frac{1}{4C} & \frac{1}{2C} & \frac{-1}{4C} \\ 0 & 0 & 0 & 0 & 0 \\ 0 & 0 & 0 & 0 & 0 \\ \frac{d_3-1}{L} & 0 & 0 & 0 & 0 \end{bmatrix} \tag{23}$$

III. CONTROL SYSTEM

A. ROBUST STABILITY OF MIMO SYSTEMS

In this section, a necessary and sufficient condition for robust stability and robust performance of MIMO systems is investigated. The general interconnected system is shown in Fig.4. Let's perturbation matrix $\tilde{\Delta}_u$ consisting of *scalar* blocks and *full* blocks, defines as (24), and $\mathcal{M}(s) = \mathcal{LLFT}(\mathcal{P}, \mathcal{K})$. Then Theorem 1 is held:

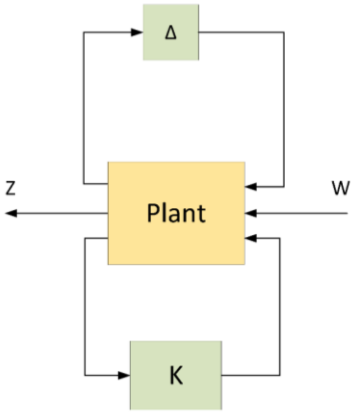

FIGURE 4. The general framework for an uncertain feedback system.

$$\tilde{\Delta}_u = \{diag[\delta_1 I_{r1}, \ldots, \delta_s I_{rs}, \Delta_1, \ldots, \Delta_F]; \ \delta_i \in \mathbb{C}, \ \Delta_j \in \mathbb{C}^{m_j \times m_j} \tag{24}$$

Theorem 1: Consider closed-loop system $\mathcal{M}(s)$ and the perturbations $\Delta(s)$ $\left(\Delta \in \tilde{\Delta}_w\right)$ where $\mathcal{M}(s)$ and $\Delta(s)$ are stable and $\tilde{\Delta}_u$ is a convex set. Then the $\mathcal{M} - \Delta$ system is stable

for all allowed perturbations if and only if $det(I-\mathcal{M}\Delta(j\omega) \neq 0 \forall \omega, \forall \Delta \in \tilde{\Delta}_u \Leftrightarrow \lambda_i(\mathcal{M}\Delta)\big) \neq 1, \forall \omega, \forall \Delta \in \tilde{\Delta}_u$.

Proof: Condition $det(I-\mathcal{M}\Delta(j\omega) \neq 0$ is derived from the extension of the Nyquist criterion for the MIMO system, which states that $\mathcal{M}-\Delta$ structure is stable if and only if

$\det(\mathrm{I}-\mathrm{M}\Delta(\mathrm{j}\omega)$ does not encircle the origin for $\forall \Delta \in \widetilde{\Delta}_{\mathrm{u}}$. The phrase $\lambda_{\mathrm{i}}(\mathcal{M}\Delta)) \neq 1$ can be proved by considering the fact that $det(\mathrm{I}-\mathcal{M}\Delta) = \prod_{i=1}^{n} \lambda_i(I-\mathcal{M}\Delta) = \prod_{i=1}^{n}(I-\lambda_i(\mathcal{M}\Delta)) \neq 0 \Rightarrow \lambda_{\mathrm{i}}(\mathcal{M}\Delta)) \neq 1$.

Theorem 2: Consider closed-loop system $\mathcal{M}(s)$ and complex $\tilde{\Delta}_u$. Then the $\mathcal{M}-\Delta$ system is stable for all allowed perturbations if and only if $\rho(\mathcal{M}\Delta(j\omega)) \equiv \max_i |\lambda_i(\mathcal{M}\Delta(j\omega))| < 1 \forall \omega, \forall \Delta \in \tilde{\Delta}_u$.

Lemma 1: Assume $\tilde{\Delta}_u$ be the set of all complex matrices (unstructured full-block matrix) such that $\bar{\sigma}(\Delta) < 1 \forall \Delta \in \tilde{\Delta}_u$. Then the $\mathcal{M}-\Delta$ system is stable if and only if $\bar{\sigma}(\mathcal{M}) < 1$.

Proof: According to the Theorem 2, the robust stability criterion is $\rho(\mathcal{M}\Delta(\mathrm{j}\omega)) < 1$. Therefore, the following inequalities hold: $\max \rho(\mathcal{M}\Delta) \leq \max \bar{\sigma}(\mathcal{M}\Delta) \leq \max \bar{\sigma}(\mathcal{M})\bar{\sigma}(\Delta) = \bar{\sigma}(\mathcal{M})$.

While Theorems 1 and 2 provide the necessary and sufficient conditions for the stability of the $\mathcal{M}-\Delta$ structure, they do not provide a methodology to identify the most critical $\Delta \in \widetilde{\Delta}_{\mathrm{u}}$ which makes the $\mathcal{M}\Delta$ unstable for $\min \|\mathcal{M}\|$. For unstructured full-block matrices Δ, Lemma 1 offers necessary and sufficient conditions for stability. However, when Δ has no structure, Lemma 1 can solely guarantee sufficient (not necessary) conditions for stability (i.e., for structured uncertainties where $\widetilde{\Delta}_{\mathrm{u}} = \mathrm{diag}\{\Delta_{\mathrm{i}}\}$ the $\mathcal{M}-\Delta$ structure is stable if $\bar{\sigma}(\mathcal{M}(j\omega)) < 1 \forall \omega$). The advantage of Lemma 1 over Theorems 1 and 2 is that the stability condition is independent of Δ. Now the question arises whether we can drive tighter bounds on stability, and find conditions close to necessary, and independent of Δ. This leads us to the structured singular value (SSV) concept and input-output scaling, which are elaborated upon in the following sections [43].

B. STRUCTURED SINGULAR VALUES AND ROBUST STABILITY

Definition 1: For an arbitrary real or complex matrix $\mathcal{M}$ the *ssv* is defined by (25).

$$\mu^{-1}_{\Delta(\mathcal{M})} \triangleq \min_{\Delta}\{\bar{\sigma}(\Delta) | \Delta \in \tilde{\Delta}_u, det(I-\mathcal{M}\Delta) = 0\} \quad (25)$$

if there is a perturbation $\Delta \in \tilde{\Delta}_u$ such that $det(I-\mathcal{M}\Delta) = 0$. Otherwise $\mu_\Delta(\mathcal{M}) = 0$.

Theorem 3: Consider a stable nominal system $\mathcal{M}$ and the perturbations Δ. Then the $\mathcal{M}-\Delta$ system with $\bar{\sigma}(\Delta) \leq 1$ is stable if and only if $\mu_\Delta(\mathcal{M}(j\omega)) \leq 1, \forall \omega$.

Computing $\mu_\Delta(\mathcal{M})$ depends on the structure of Δ and determining its value is not straightforward. Therefore, with the assistance of μ_Δ properties, upper and lower bounds of $\mu_\Delta(\mathcal{M})$ are attempted to compute. Hence, the following lemma can be derived [44]:

Lemma 2: For a perturbation Δ the following estimation for the upper and lower bounds of $\mu_\Delta(\mathcal{M})$ holds:

$$\rho(\mathcal{M}) \leq \mu_\Delta(\mathcal{M}) \leq \bar{\sigma}(\mathcal{M}) \quad (26)$$

Lemma 2 may be impractical for deriving the upper and lower bounds of $\mu_\Delta(\mathcal{M})$, due to the potentially large gap between $\rho(\mathcal{M})$ and $\bar{\sigma}(\mathcal{M})$. Fortunately, the bounds can be refined by considering transformations on M that preserve $\mu_\Delta(\mathcal{M})$ while affecting $\rho(\mathcal{M})$ and $\bar{\sigma}(\mathcal{M})$. Various algorithms, such as the $D-\mathcal{K}$ algorithm, have been proposed in the literature. When systems incorporate parametric uncertainties, the $D-\mathcal{G}-\mathcal{K}$ algorithm has demonstrated promising outcomes, which is adopted in this paper [44].

C. D–$\mathcal{G}$ – $\mathcal{K}$ METHOD

Let the perturbation matrix Δ consisting of real scalar blocks, complex scalar blocks, and full blocks.

$$\begin{aligned}\Delta = \{&diag[\varphi_1 I_{k1}, \ldots, \varphi_{sr} I_{k_{sr}}, \delta_1 I_{r1}, \ldots, \delta_s I_{rsc},\\ &\Delta_1, \ldots, \Delta_F];\\ &\delta_i \in \mathbb{C}, \ \varphi_i \in \mathbb{R}, \Delta_j \in \mathbb{C}^{m_j \times m_j}\}\end{aligned}$$

$\mu_\Delta(\mathcal{M})$ is defined as (25). To ensure the robust performance of the system there must be frequency-dependent matrices $D_\omega \in \mathfrak{D}$ and $\mathcal{G}_\omega \in \mathcal{G}$ such that:

$$\begin{aligned}&\sup_\omega \bar{\sigma}[(\frac{D_\omega \mathcal{LFFT}(\mathcal{P},\mathcal{K}) D_\omega^{-1}}{\beta} - j\mathcal{G}_\omega)(I+\mathcal{G}_\omega{}^2)^{-\frac{1}{2}}]\\ &\leq 1, \forall \omega\end{aligned} \quad (27)$$

where $\mathfrak{D}$ and $\mathcal{G}$ are defined as follows:

$$\begin{cases} \mathcal{G} = \left\{diag\left[\mathcal{G}_1, \ldots, \mathcal{G}_{s_r}, 0, \ldots, 0\right] : \mathcal{G}_i = \mathcal{G}_i{}^* \in \mathbb{C}^{k_i \times k_i}\right\} \\ \mathfrak{D} = \begin{cases} diag\left[\widetilde{D}_1, \ldots, \widetilde{D}_{s_r}, D_1, \ldots, D_{s_c}, d_1 I_{m1}, \ldots, \right. \\ \qquad I_{F-1}, I_{mF} \\ \widetilde{D}_i \in \mathbb{C}^{k_i \times k_i}, \widetilde{D}_i = \widetilde{D}_i^* > 0, d_j \in \mathbb{R}, d_j > 0 \\ \qquad D_i \in \mathbb{C}^{r_i \times r_i}, D_i = D_i^* > 0 \end{cases} \end{cases} \quad (28)$$

Hence, the $D-\mathcal{G}-\mathcal{K}$ algorithm can be outlined as follows:

1. Determine the initial matrices $D_\omega \in \mathfrak{D}$ and $\mathcal{G}_\omega \in \mathcal{G}$ and $\beta_1 > 0$, such that:

$$\begin{aligned}&\sup_\omega \bar{\sigma}[(\frac{D_\omega \mathcal{LLFF}(\mathcal{P},\mathcal{K}) D_\omega^{-1}}{\beta_1} - j\mathcal{G}_\omega)(I+\mathcal{G}_\omega{}^2)^{-\frac{1}{2}}]\\ &\leq 1\end{aligned} \quad (29)$$

Suitable initial parameters may be $D_\omega = \mathbf{I}$, $\mathcal{G}_\omega = 0$, and a large positive β.

2. Fit transfer functions $D(s)$ and $\mathcal{G}(s)$ to D_ω and $\mathcal{G}_\omega$, such that $D(j\omega) \approx D_\omega$ and $\mathcal{G}(j\omega) \approx j\mathcal{G}_\omega$. Therefore:

$$\begin{aligned}&\sup_\omega \bar{\sigma}\\ &[(\frac{D_\omega \mathcal{LLF}(\mathcal{P}(j\omega),\mathcal{K}(j\omega)) D_\omega^{-1}}{\beta_1} - jG_\omega)(I+\mathcal{G}_\omega{}^2)^{-\frac{1}{2}}]\end{aligned}$$

$$\sup_{\omega} \bar{\sigma}[(\frac{D(s)\mathcal{LLFT}(\mathcal{P}(s), \mathcal{K}(s))D(s)^{-1}}{\beta_1} - \mathcal{G}(s))(I + \widetilde{G}(s)\mathcal{G}(s))^{-\frac{1}{2}}] \quad (30)$$

3. Assume $D(s)$ be factorized such that $D(s) = D_{ap}(s)D_{min}(s)$, $\widetilde{D}_{ap}(s)D_{\boldsymbol{ap}}(s) = I$; $D_{min}(s){D_{min}}^{-1}(s) \in H_\infty$. Where $D_{ap}(s)$ is all passed and $D_{min}(s)$ is stable and minimum phase transfer matrix. Then find a normalized right coprime factorization $\widetilde{D}_{ap}(s)\mathcal{G}(s)D_{ap}(s) = \mathcal{G}_N\mathcal{G}_M^{-1}, \mathcal{G}_N, \mathcal{G}_M \in H_\infty$ such that $\widetilde{\mathcal{G}_M}\mathcal{G}_M + \widetilde{\mathcal{G}_N}\mathcal{G}_N = I$. Then $\mathcal{G}_M^{-1}\widetilde{D}_{ap}(I + \widetilde{\mathcal{G}}\mathcal{G})^{-1}D_{ap}\left(\mathcal{G}_M^{-1}\right)^{\sim} = I$. For each frequency $S = j\omega$, (31), as shown at the bottom of the next page:

4. Consider the following definition:

$$\mathcal{P}_a = \begin{bmatrix} D_{min}(s) & \\ & I \end{bmatrix} \mathcal{P}(s) \begin{bmatrix} {D_{min}}^{-1}(s)\mathcal{G}_M(s) & \\ & I \end{bmatrix} - \beta_1 \begin{bmatrix} \mathcal{G}_N & \\ & 0 \end{bmatrix} \quad (32)$$

and find a controller $\mathcal{K}_{new}$ minimizing $\overline{\|}(\mathcal{LLT}(\mathcal{P}_a, \mathcal{K}))\|_\infty$

5. Determine a New β_1

$$\begin{cases} \beta_1 = \sup_{\omega} \quad \inf_{\widetilde{D}_\omega \in \mathfrak{D}, \widetilde{G} \in \mathcal{G}} \{\beta(\omega) : \Gamma \le 1\} \\ \Gamma = \bar{\sigma}[(\frac{\widetilde{D}_\omega \mathcal{LLF}(\mathcal{P}, \mathcal{K}_{new})\widetilde{D}_\omega{}^{-1}}{\beta_1} - j\widetilde{\mathcal{G}}_\omega)(I + \widetilde{\mathcal{G}}_\omega{}^2)^{-\frac{1}{2}}] \end{cases} \quad (33)$$

6. Determine $\widehat{D_\omega}$ and $\widehat{\mathcal{G}_\omega}$ such that:

$$\inf_{\widetilde{D}\omega \in \mathfrak{D}, \widetilde{G} \in G} \bar{\sigma} [(\frac{\widehat{D_\omega}\mathcal{LLFTF}(\mathcal{P}, \mathcal{K}_{new})\widehat{D_\omega}^{-1}}{\beta_1} - j\widehat{\mathcal{G}_\omega})(I + \widehat{\mathcal{G}_\omega}^2)^{-\frac{1}{2}}] \quad (34)$$

7. Terminate the process if updated scaling matrices $\widehat{D_{\boldsymbol{\omega}}}$ and $\widehat{\mathcal{G}_{\boldsymbol{\omega}}}$ and initial $D_{\boldsymbol{\omega}}$ and $\mathcal{G}_\omega$ are sufficiently similar; otherwise, substitute D_ω, $\mathcal{G}_\omega$, and $\mathcal{K}$ with $\widehat{D_\omega}$, $\widehat{\mathcal{G}_\omega}$, and $\mathcal{K}_{\boldsymbol{new}}$, and return to step (2).

The flowchart of the $D - G - \mathcal{K}$ algorithm is presented in Figure 5, which summarizes the main steps of the $D - G - \mathcal{K}$ iterative procedure, as detailed in Section C.

D. ROBUST CONTROLLER SYNTHESIS FOR $MPDC_{3L}^{SU}$ AND $MPDC_{3L}^{SD}$

Following the discussion in section II, the objective of the robust controller synthesis is to determine state-feedback gains of the $MPDC_{3L}^{SU}$ and $MPDC_{3L}^{SD}$ while considering uncertainties in the inductors and capacitors within the interval $C = [C_{min}, C_{max}]$, $L = [L_{min}, L_{max}]$. The nominal values of C and L are given in Table 1, with an uncertainty range of $\pm 10\%$. The block diagram of the closed-loop system with performance weighting transfer functions is shown in Fig. 6, where Z1, Z2, and Z3 are exogenous outputs. Here, $\mathcal{W}_{s1,\ldots,s4}$, $\mathcal{W}_{u1,\ldots,u3}$, and $\mathcal{W}_{T1,\ldots,T4}$, represent weighting transfer functions corresponding to tracking and disturbance rejection, controller effort, and system robustness, respectively. To ensure effective reference tracking and disturbance rejection, $\mathcal{W}_{s1,\ldots,s4}$, are considered as low-pass filters with large magnitude within the control bandwidths for good reference-tracking and disturbance-rejection performance. Meanwhile, $\mathcal{W}_{u1,\ldots,u3}$ are set to a constant to limit duty cycles, $[d_{[1]}, d_{[2]}, d_{[3]}]$, and $\mathcal{W}_{T1,\ldots,T4}$, are chosen as high-pass filters with low DC gain for robustness and noise attenuation. Sensor noise attenuation weighting functions are designed to effectively suppress system sensitivity within the frequency range where sensor noise is typically present, primarily in the high-frequency spectrum. A first-order high-pass filter is employed for this purpose, enabling the attenuation of high-frequency disturbances introduced by sensor noise. Additionally, $\mathcal{W}_{I1,\ldots,I4}$ determine limitations on $\left[v_i, v_{[1]}^{ref}, v_{[2]}^{ref}, v_{[3]}^{ref}\right]$.

The converter topologies $MPDC_{3L}^{SU}$ and $MPDC_{3L}^{SD}$, exhibit RHP zeros. This non-minimum phase behavior imposes fundamental limitations on control design by constraining the achievable bandwidth and shaping the overall closed-loop response. Increasing bandwidth beyond a certain point can lead to instability, making it essential to strike a careful balance between fast dynamics and system stability [45], [46].

Beyond bandwidth limitations, RHP zeros influence several critical aspects of system performance, including overshoot, settling time, and disturbance rejection. These trade-offs become especially significant when fast transient behavior is desired, as it may come at the cost of reduced- robustness or increased sensitivity to model uncertainties [45], [46]. With these constraints in mind, the control strategies developed for the proposed converters are specifically designed to maintain both dynamic performance and robust stability.

Fig.7 shows the singular value plot over frequency for the $MPDC_{3L}^{SU}$. Initially, the frequency distribution of μ is non-uniform with a peak μ value of 7.836. Subsequently, through further design iterations, the μ values become uniform across a wide frequency range, and the peak of μ value decreases to 0.833. This reduction in the peak of μ value indicates improved robust stability and robust performance. The initially designed controller has a high order of 39. To reduce the controller's order, Hankel singular values are utilized. As evident from Fig. 8, the first 9 Hankel singular values are notably greater than the others. Therefore, the controller's order can be effectively reduced to nine. The comparison between the initial controller and its reduced order is illustrated in Fig. 9.

In the conventional μ method, parametric uncertainties are typically represented by complex uncertainties to facilitate- analysis and synthesis with the iterative $D - \mathcal{K}$ algorithm. However, this often leads to conservative controller designs. In contrast, the mixed μ analysis and synthesis method consider all parametric uncertainties in their real form. This approach analyzes and synthesizes the system with the iterative $D - \mathcal{G} - \mathcal{K}$ method, resulting in a less

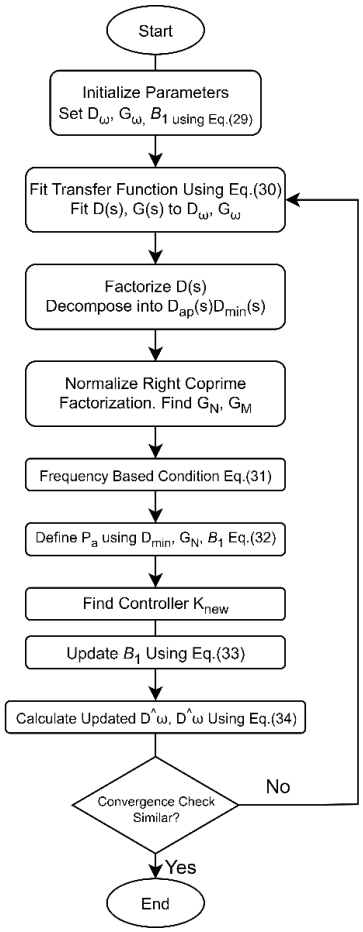

FIGURE 5. D-G-K algorithm flowchart.

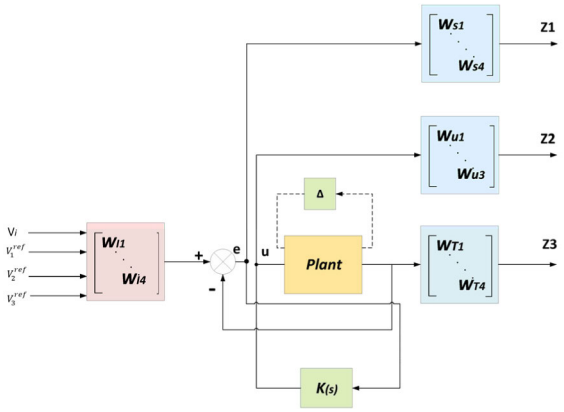

FIGURE 6. Augmented plant.

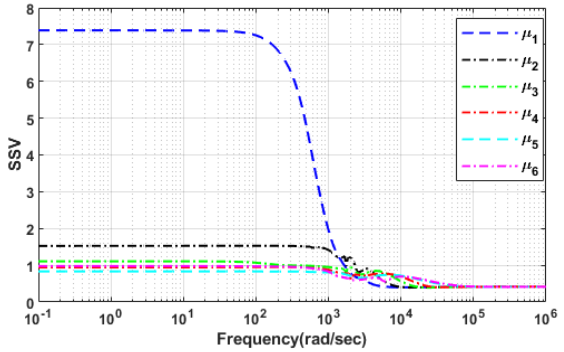

FIGURE 7. Structure singular values of $MPDC_{3L}^{SU}$.

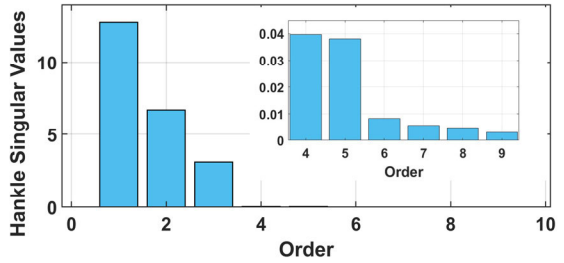

FIGURE 8. Hankel singular values of $MPDC_{3L}^{SU}$.

conservative solution and offering proper robust performance [44]. To compare these two approaches, the worst-case disturbance rejection responses are illustrated in Fig. 10. It is evident that considering real uncertainties results in a less conservative solution and offers proper robust performance. Fig.11 shows the singular value plot over frequency for the $MPDC_{3L}^{SD}$. Initially, the frequency distribution of μ is non-uniform with a peak μ value of 4.94. Subsequently, through further design iterations, the μ values become uniform across a wide frequency range, and the peak of μ value decreases to 0.606. This reduction in the peak

$$
\begin{aligned}
&\bar{\sigma}[(\frac{D(s)\mathcal{LLFT}(\mathcal{P}(s),\mathcal{K}(s))D(s)^{-1}}{\beta_1} - \mathcal{G}(s))(I+\widetilde{\mathcal{G}}(s)\mathcal{G}(s))^{-\frac{1}{2}}]\\
&\approx \bar{\sigma}[(\frac{D_{min}\mathcal{LLFT}(\mathcal{P},\mathcal{K})D_{min}{}^{-1}}{\beta_1} - \widetilde{D}_{ap}\mathcal{G}D_{ap})\widetilde{D}_{ap}(I+\widetilde{\mathcal{G}}\mathcal{G})^{-\frac{1}{2}}]\\
&= \bar{\sigma}[(\frac{D_{min}\mathcal{LLFT}(\mathcal{P},\mathcal{K})D_{min}{}^{-1}}{\beta_1} - \mathcal{G}_N\mathcal{G}_M^{-1})\widetilde{D}_{ap}(I+\widetilde{\mathcal{G}}\mathcal{G})^{-\frac{1}{2}}]\\
&= \bar{\sigma}[(\frac{D_{min}\mathcal{LLFT}(\mathcal{P},\mathcal{K})D_{min}{}^{-1}}{\beta_1} - \mathcal{G}_N)\mathcal{G}_M^{-1}\widetilde{D}_{ap}(I+\widetilde{\mathcal{G}}\mathcal{G})^{-\frac{1}{2}}]\\
&= \bar{\sigma}[(\frac{D_{min}\mathcal{LLFT}(\mathcal{P},\mathcal{K})D_{min}{}^{-1}}{\beta_1} - \mathcal{G}_N].
\end{aligned}
\tag{31}
$$

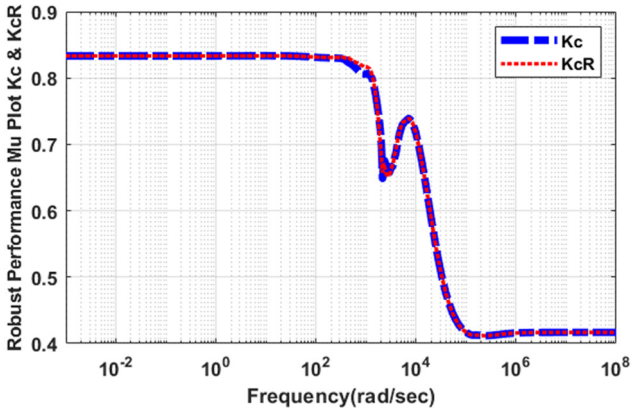

FIGURE 9. Robust performance comparison of $MPDC_{3L}^{SU}$.

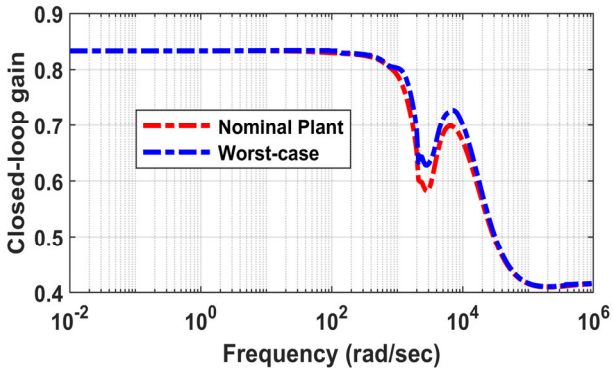

FIGURE 10. Worst-case disturbance rejection response of $MPDC_{3L}^{SU}$.

of μ value signifies improved robust stability and robust performance.

The initial controller has an order of 26. To reduce the controller's order, Hankel singular values are utilized. As depicted in Fig. 12, the first 8 Hankel singular values are notably greater than the others. Therefore, the controller's order can be effectively reduced to 8. The comparison between the initial controller and its reduced order is illustrated in Fig. 13.

IV. RESULTS AND DISCUSSION

A. HIL TEST RESULTS

Fig. 14 shows the laboratory setup. The experimental platform is based on the OPAL-RT 4610XG real-time simulator, which features a Xilinx® Kintex®-7 410T FPGA and an AMD Ryzen™ 6-core, 3.8 GHz processor. Within this framework, the converter models for the $MPDC_{3L}^{SU}$ and $MPDC_{3L}^{SD}$ are executed on the FPGA, while the robust controllers are implemented on the CPU. The eHS, the Opal-RT real-time FPGA-based solver, operates with a step time of 120 ns, while the CPU step time is set to 20μs.

To assess the effectiveness of the robust controller, different scenarios are defined. In the first scenario, $MPDC_{3L}^{SU}$ operates under normal conditions where the loads R_2 and R_3, as specified in Table 1, are at their nominal values,

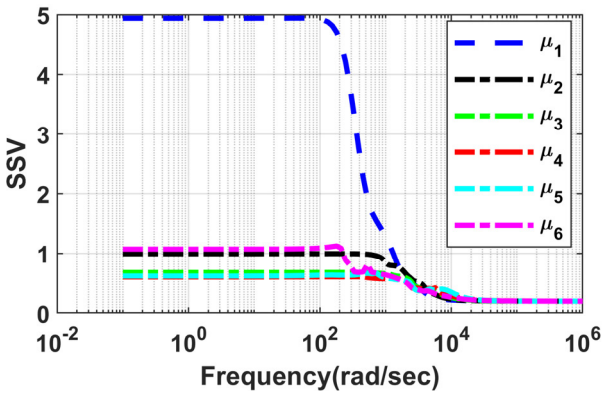

FIGURE 11. Structure singular values of $MPDC_{3L}^{SD}$.

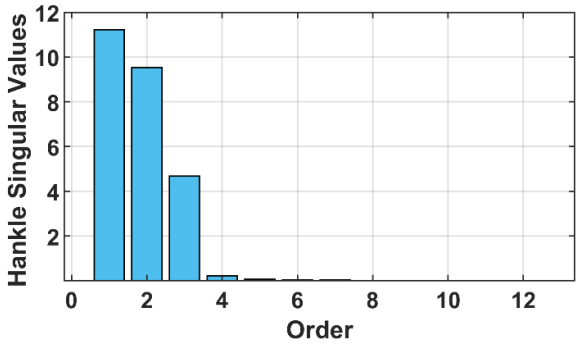

FIGURE 12. Hankel singular values of $MPDC_{3L}^{SD}$.

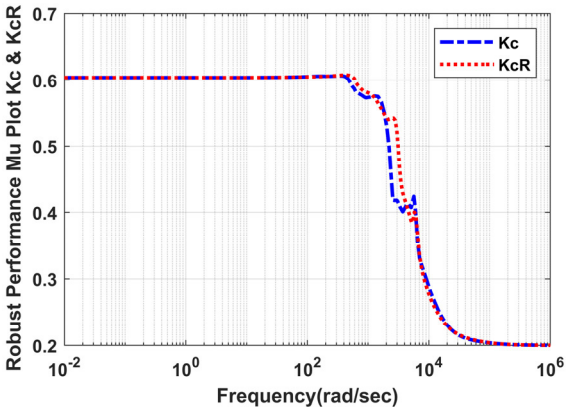

FIGURE 13. Robust performance comparison of $MPDC_{3L}^{SD}$.

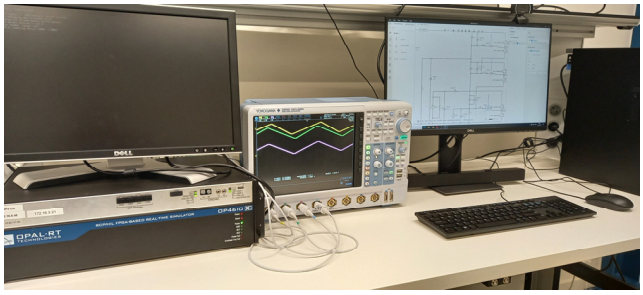

FIGURE 14. Experimental HIL setup; OPAL-RT 4610.

consuming P = 279W and P = 131W, respectively. During this period, the current source $I_{s[1]}$ and voltage source v_i supply P = 239W and P = 174W, respectively. Then,

TABLE 1. Parameters of 3-level MMPC.

$MPDC_{3L}^{SU}$		$MPDC_{3L}^{SD}$		Common Parameters	
Parameters	Value	Parameters	Value	Parameters	Value
v_i	48v	v_i	240v	C	100µF
$v_{[1]}^{ref}$	120v	$v_{[0]}^{ref}$	48v	L	570µH
$v_{[2]}^{ref}$	180v	$v_{[1]}^{ref}$	120v	f	20kHz
$v_{[3]}^{ref}$	240v	$v_{[2]}^{ref}$	180v		
R_2	116Ω	R_2	57Ω		
R_3	440Ω	R_0	5Ω		
$I_{s[1]}$	2A	$I_{s[1]}$	2A		

TABLE 2. Steady-state values for 3-Level MMPC.

$MPDC_{3L}^{SU}$		$MPDC_{3L}^{SD}$	
Parameters	Value	Parameters	Value
$I_{L[1]}$	5.9A	$I_{L[1]}$	12.6A
$I_{L[2]}$	4.9A	$I_{L[2]}$	6.4A
$I_{L[3]}$	1.1A	$I_{L[3]}$	6.6A
$I_{[2]}$	1.5A	$I_{[2]}$	3.2A
$I_{[3]}$	0.5A	$I_{[0]}$	9.7A

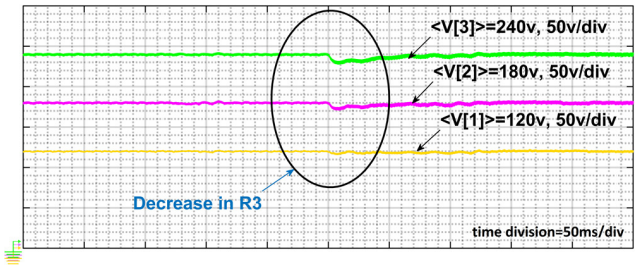

FIGURE 15. Steady-state and transient waveform of output voltages [$v_{[1]}$, $v_{[2]}$, $v_{[3]}$] of $MPDC_{3L}^{SU}$ under nominal and load changed conditions.

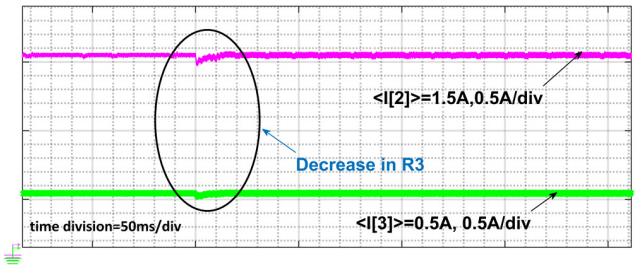

FIGURE 16. The output currents [$I_{[2]}$, $I_{[3]}$] of $MPDC_{3L}^{SU}$ when R_3 is nominal value and changed by half.

to evaluate the transient response of the controller, the load R_3 is suddenly reduced by half, while the load R_2 remains unchanged. Fig.15 shows the steady-state and transient waveforms of output voltages [$v_{[1]}$, $v_{[2]}$, $v_{[3]}$] for the $MPDC_{3L}^{Su}$ under nominal and load change conditions. As is observed, output voltages, [$v_{[1]}$, $v_{[2]}$, $v_{[3]}$], perfectly tracked the-reference voltages $\left[v_{[1]}^{ref}, v_{[2]}^{ref}, v_{[3]}^{ref}\right]$ following an acceptable undershoot during the R_3 alteration, demonstrating effective tracking performance. Fig. 16 and Fig. 17 show dynamic and steady-state waveforms of output currents [$I_{[2]}$, $I_{[3]}$], and inductors current [$I_{L[1]}$, $I_{L[2]}$, $I_{L[3]}$], respectively. The measurements of output currents [$I_{[2]}$, $I_{[3]}$], As well as inductors

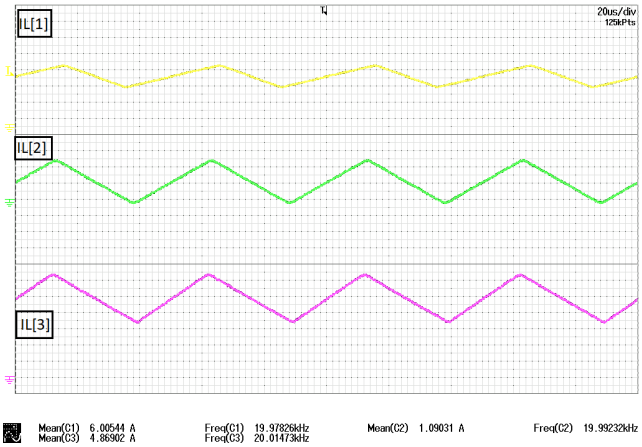

FIGURE 17. The inductors current [$I_{L[1]}$, $I_{L[2]}$, $I_{L[3]}$] of $MPDC_{3L}^{SU}$ under nominal conditions.

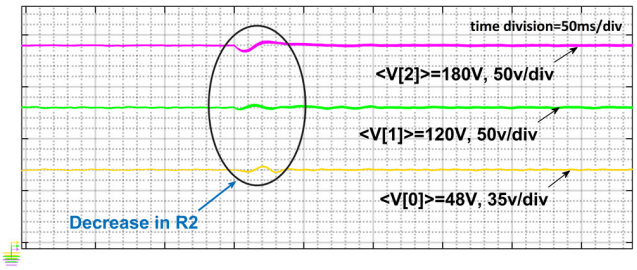

FIGURE 18. Steady-state and transient waveform of output voltages [$v_{[1]}$, $v_{[2]}$, $v_{[3]}$] of $MPDC_{3L}^{SD}$ under nominal and load change conditions.

FIGURE 19. The inductor's current [$I_{L[1]}$, $I_{L[2]}$, $I_{L[3]}$] of $MPDC_{3L}^{SD}$ under nominal conditions.

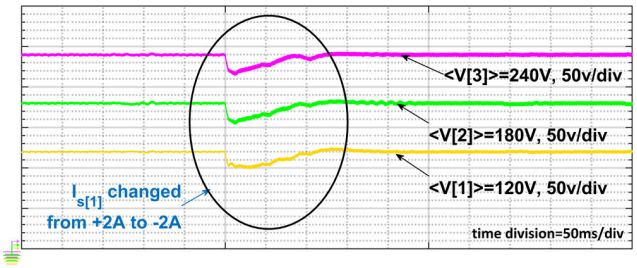

FIGURE 20. Bidirectional operation of the $MPDC_{3L}^{SU}$. The output voltages [$v_{[1]}$, $v_{[2]}$, $v_{[3]}$], when $I_{s[1]}$ changed from +2A to −2A.

current [$I_{L[1]}$, $I_{L[2]}$, $I_{L[3]}$] are provided in Table 2. When the load R_3 was altered, the inductors current become $I_{L[1]}$ =

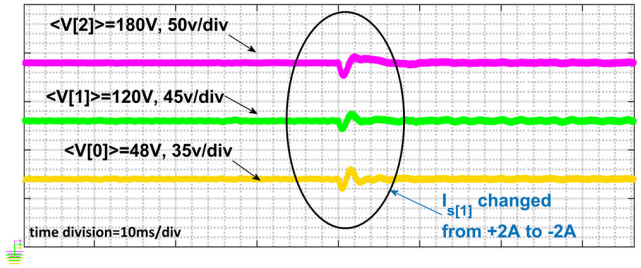

FIGURE 21. Bidirectional operation of the $MPDC_{3L}^{SD}$. The output voltages [$v_{[1]}$, $v_{[2]}$, $v_{[3]}$], when $I_{s[1]}$ changed from +2A to −2A.

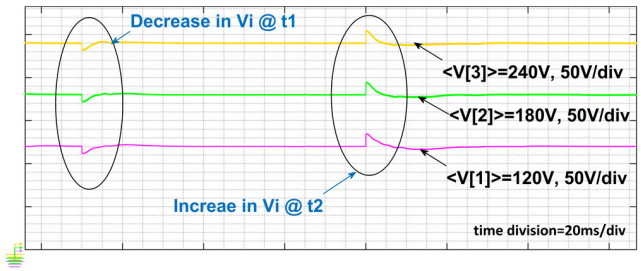

FIGURE 22. Steady-state and transient waveform of output voltages [$v_{[1]}$, $v_{[2]}$, $v_{[3]}$] of $MPDC_{3L}^{SU}$ under nominal conditions, and input voltage alternation.

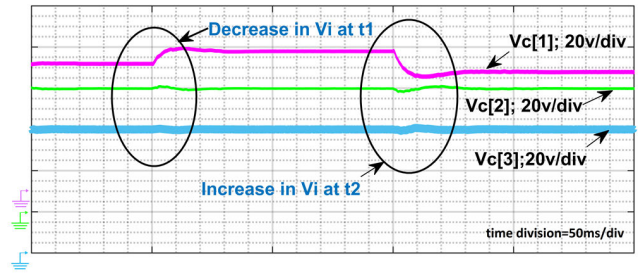

FIGURE 23. Steady-state and transient waveform of capacitors voltages [$v_{C[1]}$, $v_{C[2]}$, $v_{C[3]}$] of $MPDC_{3L}^{SU}$ under nominal condition, and input voltage alternation.

9.6A, $I_{L[2]} = 6.9A$, *and* $I_{L[3]} = 2.2A$, while the current source $I_{s[1]}$ and the voltage source v_i, supply P=240W and P=310W, respectively. Fig.18 shows the steady-state and transient waveforms of output voltages [$v_{[0]}$, $v_{[1]}$, $v_{[2]}$] for the $MPDC_{3L}^{SD}$ under nominal conditions, as specified in Table (1), and when R_2 is suddenly halved. As is observed, output voltages, [$v_{[0]}$, $v_{[1]}$, $v_{[2]}$], perfectly tracked the reference voltages $\left[v_{[0]}^{ref}, v_{[1]}^{ref}, v_{[2]}^{ref}\right]$. During nominal conditions, R_2 and R_0 consuming P = 565W and P = 463W, respectively, while the current source $I_{s[1]}$ and voltage source v_i supply P = 239W and P = 804W, respectively. The measurements of output currents [$I_{[0]}$, $I_{[2]}$], as well as inductors' current [$I_{L[1]}$, $I_{L[2]}$, $I_{L[3]}$] are provided in Table 2. Fig. 19 shows steady-state waveforms of inductors current [$I_{L[1]}$, $I_{L[2]}$, $I_{L[3]}$]. When the load R_2 was altered, the inductor's current become $I_{L[1]} = 13.9A$, $I_{L[2]} = 9.2A$, and $I_{L[3]} = 11.3A$, while the output currents become $I_{[0]} = 9.7A$, and $I_{[2]} = 6.3A$. Meanwhile, the current source $I_{s[1]}$ and the voltage source v_i supply P = 240W and P = 1130W, respectively.

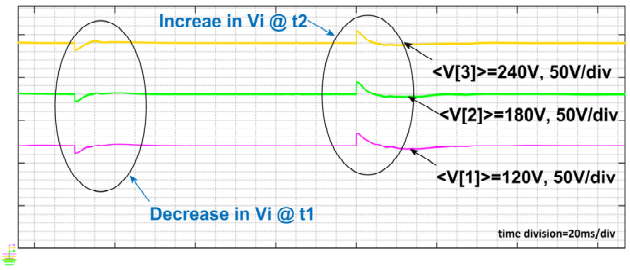

FIGURE 24. Steady-state and transient waveform of output voltages [$v_{[1]}$, $v_{[2]}$, $v_{[3]}$] of $MPDC_{3L}^{SU}$ under input voltage alternation.

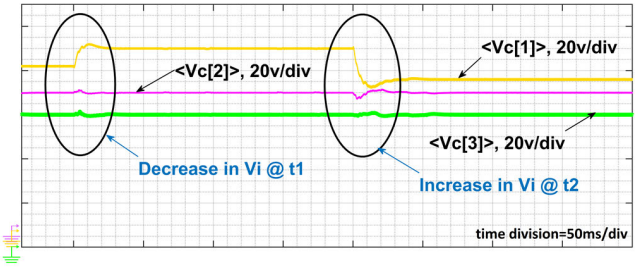

FIGURE 25. Steady-state and transient waveform of capacitors voltages [$v_{C[1]}$, $v_{C[2]}$, $v_{C[3]}$] of $MPDC_{3L}^{SU}$ under input voltage alternation.

FIGURE 26. Experimental setup.

In the second scenario, by a sudden change of the current source $I_{s[1]}$ from +2A to −2A, the bidirectional capability of the $MPDC_{3L}^{SU}$ and $MPDC_{3L}^{SD}$ is explored. Fig. 20 and Fig. 21 show the corresponding output voltages [$v_{[1]}$, $v_{[2]}$, $v_{[3]}$] for the $MPDC_{3L}^{Su}$ and $MPDC_{3L}^{SD}$, respectively. These figures demonstrate rapid convergence and minimal oscillations, indicating the effectiveness of the proposed controller.

Feature	μ-Synthesis	H_∞ Control	Robust Optimal LQR Control (Lyapunov-based)	Adaptive Robust Control	Robust Model Predictive Control
Design Approach	Uses $D-\mathcal{G}-\mathcal{K}$ iteration to minimize the μ, ensuring robust stability and performance in uncertain systems.	Optimizes the control law to minimize the worst-case disturbance gain H_∞	Solves a Riccati equation based on a Lyapunov function to ensure stability and optimize performance.	Adjusts control parameters in real time to adaptively handle system uncertainties.	Optimizes control inputs over a prediction horizon while considering constraints and uncertainties.
Robustness to Uncertainty	Handles both structured and unstructured uncertainties; worst-case design.	Unstructured uncertainties, with limited handling of structured uncertainties.	Offers robustness to matched uncertainties and parameter variations within the Lyapunov stability region.	Adaptively handles unstructured uncertainties; struggles with structured ones.	Handles structured uncertainties; less effective for fast or unstructured uncertainty.
Computational Complexity	Moderate; offline iterative $D-\mathcal{G}-\mathcal{K}$ optimization.	Moderate; H_∞ frequency-domain optimization.	Moderate; offline Riccati equation solution, low runtime computational burden.	High; requires real-time parameter estimation and update laws.	High; online optimization is needed at every step.
Implementation	Low-order controller with fixed gain matrix; relatively straightforward.	Relatively low-order controller with a fixed gain matrix; frequency-domain design.	Straightforward; provides state feedback control law, easily implemented once designed.	Complex; requires online adaptation mechanisms.	Complex; requires real-time solvers and accurate models.
Disadvantages	No adaptability; conservative due to worst-case design.	Limited to unstructured uncertainty; not adaptive.	Assumes full state feedback; performance may degrade outside design region; sensitivity to model inaccuracy.	Complex; may respond slowly to fast transients.	High computational demand; model dependency.

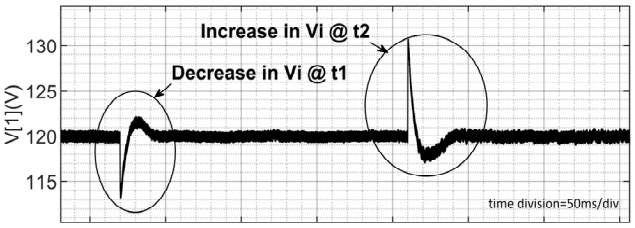

FIGURE 27. Steady-state and transient waveform of output voltage $v_{[1]}$ of $MPDC_{3L}^{SU}$ under nominal condition, and input voltage alternation.

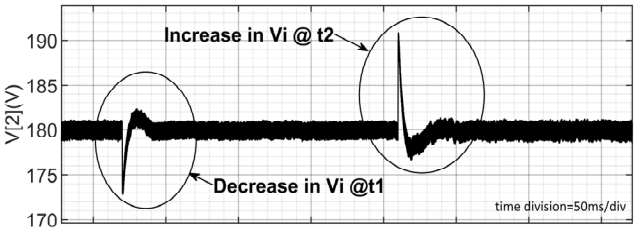

FIGURE 28. Steady-state and transient waveform of output voltage $v_{[2]}$ of $MPDC_{3L}^{SU}$ under nominal condition, and input voltage alternation.

In the third scenario, $MPDC_{3L}^{SU}$ operates under normal conditions, when at t $= t_1$ voltage source v_i is dropped from 48 V to 42 V, and at t $= t_2$ voltage source v_i is jumped from 42 V to 52 V. As is observed from Fig. 22, output voltages, $[v_{[1]}, v_{[2]}, v_{[3]}]$, perfectly tracked the reference voltages $\left[v_{[1]}^{ref}, v_{[2]}^{ref}, v_{[3]}^{ref}\right]$, demonstrating effective performance.

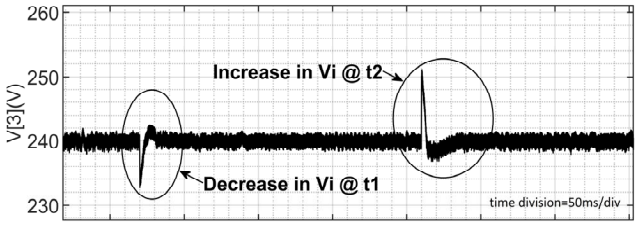

FIGURE 29. Steady-state and transient waveform of output voltage $v_{[3]}$ of $MPDC_{3L}^{SU}$ under nominal condition, and input voltage alternation.

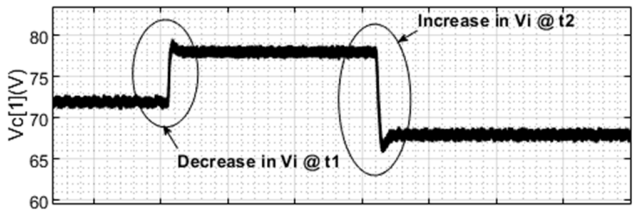

FIGURE 30. Steady-state and transient waveform of capacitor voltage $v_{C[1]}$ of $MPDC_{3L}^{SU}$ under nominal condition, and input voltage alternation.

Fig. 23 depicts steady-state and transient waveforms of capacitors voltages $[v_{C[1]}, v_{C[2]}, v_{C[3]}]$. During time interval of $(0,t_1)$, the average capacitor voltages are $v_{C[1]} = 72\ v$, $v_{C[2]} = 60\ v$, and $v_{C[3]} = 60\ v$. As v_i decreases at $t = t_1$, the average capacitor voltages become $v_{C[1]} = 78\ v$, $v_{C[2]} = 60\ v$, and $v_{C[3]} = 60\ v$, while at $t = t_2$, the average capacitor voltages become $v_{C[1]} = 68\ v$, $v_{C[2]} = 60\ v$,

$v_{C[3]} = 60\ v$. Therefore, from Fig.123, capacitor voltages $[v_{C[1]}, v_{C[2]}, v_{C[3]}]$ are adjusted such that the output voltages $[v_{[1]}, v_{[2]}, v_{[3]}]$ tracked the reference voltages $\left[v_{[1]}^{ref}, v_{[2]}^{ref}, v_{[3]}^{ref}\right]$, as is depicted in Fig.22.

In the fourth scenario, the capacitance and inductance values are reduced by 10% from their nominal values. Then at $t = t_1$ voltage source v_i is dropped from 48 V to 42 V, and at t = t_2 voltage source v_i is jumped from 42 V to 52 V. Fig. 24 shows the output voltages, $[v_{[1]}, v_{[2]}, v_{[3]}]$ of $MPDC_{3L}^{SU}$ and Fig. 25 shows steady-state and transient waveform of capacitors voltages $[v_{C[1]}, v_{C[2]}, v_{C[3]}]$.

B. EXPERIMENTAL TEST

Fig.26 shows the experimental setup to validate the proposed control method for $MPDC_{3L}^{SU}$ Three half-bridge IGBT modules, Imperix PEB4046, were employed as active switches. The synthesized robust controller was implemented on a dSPACE DS1202 MicroLabBox platform using ControlDesk software. Real-time control was achieved through a designed interface and protection interface (IPC). Current and voltage measurements were conducted using Hall effect sensors (LEM LA 55-P and LEM LV25-P models). The DC power supply was an EA-PS 9300-40, 5 kW model, as voltage source v_i while an APM SP800VDC, 4 kW model was utilized as the current source $I_{s[1]}$. The DC loads used were an EA-EL 9400-50 (2.4 kW) for R_2 and an EA-EL 9360-120B (5.4 kW) for R_3.

The experimental test is conducted to evaluate the performance of the control system under varying input voltage conditions, similar to the third scenario described in section V.A. The $MPDC_{3L}^{SU}$ operates under normal conditions. Then, at $t = t_1$ the voltage source v_i is dropped from 48 V to 42 V, and at $t = t_2$ the voltage source v_i is increased from 42 V to 52 V. The corresponding $[v_{[1]}, v_{[2]}, v_{[3]}]$, and $v_{C[1]}$, are shown in Figs. 27–30. The measurements presented in Figs. 27–30 demonstrate excellent agreement with the Opal-RT HIL test results shown in Figs. 22–23. As observed, the control system exhibits satisfactory dynamic responses, minimal oscillations around the operating point, and rapid convergence speed.

V. CONCLUSION

This paper presents a comprehensive investigation into the development of robust control strategies for MMPCs. These converters are increasingly important in modern multi-energy systems due to their ability to integrate various energy sources. However, their inherently complex structure, along with the presence of parametric uncertainties, operating disturbances, and dynamic conditions, introduces significant challenges in ensuring reliable, stable, and high-performance operation. In this study, the dynamic equations of the n-level MMPC in both step-up and step-down configurations were derived, along with the large-signal and small-signal dynamic equations for the 3-level structure. To control the converter in the presence of uncertainties, a robust μ−controller was synthesized using the $D - \mathcal{G} - \mathcal{K}$ iterative procedure. SSV analysis confirmed robust stability and performance across worst-case uncertainty scenarios, demonstrating the suitability of this approach for high-reliability and mission-critical applications. The HIL test conducted using Opal-RT, along with the experimental tests under various scenarios, demonstrated satisfactory robust performance of the MMPC during both normal operation and disturbance conditions.

APPENDIX A

Comparison of the Robust Control Methods derived as shown at the top of the previous page.

REFERENCES

[1] G. Wang, H. Wen, P. Xu, W. Liu, J. Zhou, and Y. Yang, "A comprehensive review of integrated three-port DC–DC converters with key performance indices," *IEEE Trans. Power Electron.*, vol. 39, no. 5, pp. 6391–6408, May 2024, doi: 10.1109/TPEL.2024.3366915.

[2] S. Farajdadian, A. Hajizadeh, and M. Soltani, "Recent developments of multiport DC/DC converter topologies, control strategies, and applications: A comparative review and analysis," *Energy Rep.*, vol. 11, pp. 1019–1052, Jun. 2024, doi: 10.1016/j.egyr.2023.12.054.

[3] A. K. Bhattacharjee, N. Kutkut, and I. Batarseh, "Review of multiport converters for solar and energy storage integration," *IEEE Trans. Power Electron.*, vol. 34, no. 2, pp. 1431–1445, Feb. 2019, doi: 10.1109/TPEL.2018.2830788.

[4] S. M. Taheri, A. Baghramian, and S. A. Pourseyedi, "A novel high-step-up SEPIC-based nonisolated three-port DC–DC converter proper for renewable energy applications," *IEEE Trans. Ind. Electron.*, vol. 70, no. 10, pp. 10114–10122, Oct. 2023, doi: 10.1109/TIE.2022.3220909.

[5] M. M. Haque, P. J. Wolfs, S. Alahakoon, M. A. Islam, M. Nadarajah, F. Zare, and O. Farrok, "Three-port converters for energy conversion of PV-BES integrated systems—A review," *IEEE Access*, vol. 11, pp. 6551–6573, 2023, doi: 10.1109/ACCESS.2023.3235924.

[6] H. Shayeghi, S. Pourjafar, and S. M. Hashemzadeh, "A switching capacitor based multi-port bidirectional DC–DC converter," *IET Power Electron.*, vol. 14, no. 9, pp. 1622–1636, Jul. 2021, doi: 10.1049/pel2.12137.

[7] R. Faraji, E. Adib, and H. Farzanehfard, "Soft-switched non-isolated high step-up multi-port DC–DC converter for hybrid energy system with minimum number of switches," *Int. J. Electr. Power Energy Syst.*, vol. 106, pp. 511–519, Mar. 2019, doi: 10.1016/j.ijepes.2018.10.038.

[8] S. Hasanpour, Y. P. Siwakoti, and F. Blaabjerg, "A new high efficiency high step-up DC/DC converter for renewable energy applications," *IEEE Trans. Ind. Electron.*, vol. 70, no. 2, pp. 1489–1500, Feb. 2023, doi: 10.1109/TIE.2022.3161798.

[9] X. Zhu, "A modular multiport DC–DC converter with MVDC integration for multiple DC units," *CPSS Trans. Power Electron. Appl.*, vol. 9, no. 1, pp. 99–111, Mar. 2024, doi: 10.24295/cpsstpea.2023.00047.

[10] X. Zhu, P. Hou, and B. Zhang, "A multiport current-fed IIOS dual-half-bridge converter for distributed photovoltaic MVDC integration system," *IEEE Trans. Ind. Electron.*, vol. 71, no. 4, pp. 3788–3800, Apr. 2024, doi: 10.1109/TIE.2023.3274882.

[11] F. Wu, G. Hu, J. Su, and G. Wang, "Power decoupled three-port isolated DC–DC converter based on MMC and optimization design of submodule capacitance and arm inductance," *IEEE Trans. Transport. Electrific.*, vol. 10, no. 2, pp. 4095–4106, Jun. 2024, doi: 10.1109/TTE.2023.3314449.

[12] A. Vettuparambil, K. Chatterjee, and B. G. Fernandes, "A modular multi-port converter to integrate multiple solar photo-voltaic (PV) modules with a battery storage system and a DC microgrid," *IEEE Trans. Ind. Electron.*, vol. 69, no. 5, pp. 4869–4878, May 2022, doi: 10.1109/TIE.2021.3082063.

[13] G. J. Kish, "On the emerging class of non-isolated modular multilevel DC–DC converters for DC and hybrid AC–DC systems," *IEEE Trans. Smart Grid*, vol. 10, no. 2, pp. 1762–1771, Mar. 2019, doi: 10.1109/TSG.2017.2777473.

[14] Z. Saadatizadeh, P. C. Heris, and H. A. Mantooth, "Modular expandable multiinput multioutput (MIMO) high step-up transformerless DC–DC converter," *IEEE Access*, vol. 10, pp. 53124–53142, 2022, doi: 10.1109/ACCESS.2022.3175876.

[15] K. Filsoof and P. W. Lehn, "A bidirectional multiple-input multiple-output modular multilevel DC–DC converter and its control design," *IEEE Trans. Power Electron.*, vol. 31, no. 4, pp. 2767–2779, Apr. 2016, doi: 10.1109/TPEL.2015.2448112.

[16] L. Sun, X. Xue, S. Zhang, H. Lv, and Y. Zhang, "A gridded modular bidirectional high voltage gain soft-switching DC–DC converter and its multiport expansion," *IET Power Electron.*, vol. 15, no. 6, pp. 487–503, May 2022, doi: 10.1049/pel2.12241.

[17] L. Sun, Y. Miao, J. Jia, and Y. Zhang, "Modular high conversion ratio soft-switching DC–DC converters with extended multi-ports structure for multi-energy storage systems interconnection," *J. Energy Storage*, vol. 76, Jan. 2024, Art. no. 109830, doi: 10.1016/j.est.2023.109830.

[18] M. T. Elrais, M. Safayatullah, and I. Batarseh, "Generalized architecture of a GaN-based modular multiport multilevel flying capacitor converter," *IEEE Trans. Power Electron.*, vol. 38, no. 8, pp. 9818–9838, Aug. 2023, doi: 10.1109/TPEL.2023.3269800.

[19] S. H. Kung and G. J. Kish, "Multiport modular multilevel converter for DC systems," *IEEE Trans. Power Del.*, vol. 34, no. 1, pp. 73–83, Feb. 2019, doi: 10.1109/TPWRD.2018.2846264.

[20] F. Qin, T. Hao, F. Gao, T. Xu, D. Niu, and Z. Ma, "A multiport DC–DC modular multilevel converter for HVDC interconnection," in *Proc. IEEE Appl. Power Electron. Conf. Expo. (APEC)*, Mar. 2020, pp. 520–524, doi: 10.1109/APEC39645.2020.9124277.

[21] F. M. Alhuwaishel, A. K. Allehyani, S. A. S. Al-Obaidi, and P. N. Enjeti, "A medium-voltage DC-collection grid for large-scale PV power plants with interleaved modular multilevel converter," *IEEE J. Emerg. Sel. Topics Power Electron.*, vol. 8, no. 4, pp. 3434–3443, Dec. 2020, doi: 10.1109/JESTPE.2019.2934736.

[22] M. E. S. Mahmoodieh, E. Babaei, and M. Sabahi, "A modular isolated battery-integrated multiport step-up DC–DC converter for hybrid energy applications," *IET Power Electron.*, vol. 15, no. 16, pp. 1785–1799, Dec. 2022, doi: 10.1049/pel2.12345.

[23] M. van de Wal and B. de Jager, "A review of methods for input/output selection," *Automatica*, vol. 37, no. 4, pp. 487–510, Apr. 2001, doi: 10.1016/s0005-1098(00)00181-3.

[24] K. Wang, W. Liu, and F. Wu, "Topology-level power decoupling three-port isolated current-fed resonant DC–DC converter," *IEEE Trans. Ind. Electron.*, vol. 69, no. 5, pp. 4859–4868, May 2022, doi: 10.1109/TIE.2021.3082066.

[25] E. Naghoosi and B. Huang, "Interaction analysis of multivariate control systems under Bayesian framework," *IEEE Trans. Control Syst. Technol.*, vol. 25, no. 5, pp. 1644–1655, Sep. 2017, doi: 10.1109/TCST.2016.2623281.

[26] L. Bakule, "Decentralized control: An overview," *Annu. Rev. Control*, vol. 32, no. 1, pp. 87–98, Apr. 2008, doi: 10.1016/j.arcontrol.2008.03.004.

[27] G. Galdos, A. Karimi, and R. Longchamp, "H_∞ controller design for spectral MIMO models by convex optimization," *J. Process Control*, vol. 20, no. 10, pp. 1175–1182, Dec. 2010, doi: 10.1016/j.jprocont.2010.07.006.

[28] P. Husek, "Decentralized PI controller design based on phase margin specifications," *IEEE Trans. Control Syst. Technol.*, vol. 22, no. 1, pp. 346–351, Jan. 2014, doi: 10.1109/TCST.2013.2248060.

[29] S. Khandelwal and K. P. Detroja, "The optimal detuning approach based centralized control design for MIMO processes," *J. Process Control*, vol. 96, pp. 23–36, Dec. 2020, doi: 10.1016/j.jprocont.2020.10.006.

[30] M. Veerachary, M. M. Mohan, and B. A. Reddy, "Centralized digital controller for two-input integrated DC–DC converter," in *Proc. IEEE 10th Int. Conf. Power Electron. Drive Syst. (PEDS)*, Apr. 2013, pp. 244–249, doi: 10.1109/PEDS.2013.6527022.

[31] A. Mallik and A. Khaligh, "A high step-down dual output nonisolated DC/DC converter with decoupled control," *IEEE Trans. Ind. Appl.*, vol. 54, no. 1, pp. 722–731, Jan. 2018, doi: 10.1109/TIA.2017.2757447.

[32] F. Nejabatkhah, S. Danyali, S. H. Hosseini, M. Sabahi, and S. M. Niapour, "Modeling and control of a new three-input DC–DC boost converter for hybrid PV/FC/battery power system," *IEEE Trans. Power Electron.*, vol. 27, no. 5, pp. 2309–2324, May 2012, doi: 10.1109/TPEL.2011.2172465.

[33] S. Bandyopadhyay, Z. Qin, and P. Bauer, "Decoupling control of multiactive bridge converters using linear active disturbance rejection," *IEEE Trans. Ind. Electron.*, vol. 68, no. 11, pp. 10688–10698, Nov. 2021, doi: 10.1109/TIE.2020.3031531.

[34] Z. Qian, O. Abdel-Rahman, and I. Batarseh, "An integrated four-port DC/DC converter for renewable energy applications," *IEEE Trans. Power Electron.*, vol. 25, no. 7, pp. 1877–1887, Jul. 2010, doi: 10.1109/TPEL.2010.2043119.

[35] C. S. Rios, F. G. Nogueira, B. C. Torrico, and W. B. Junior, "Robust control of a DC–DC three-port isolated converter," *Trans. Inst. Meas. Control*, vol. 43, no. 12, pp. 2658–2675, Aug. 2021, doi: 10.1177/01423312211002928.

[36] J. Garrido, F. Vázquez, and F. Morilla, "Centralized multivariable control by simplified decoupling," *J. Process Control*, vol. 22, no. 6, pp. 1044–1062, Jul. 2012, doi: 10.1016/j.jprocont.2012.04.008.

[37] A. H. A. Adam, J. Chen, M. Xu, S. Kamel, G. I. Y. Mustafa, Z. A. Zaki, and E. M. Ahmed, "Power decoupling enhancement of a triple active bridge converter with feedforward compensation based on model predictive control and fuzzy logic controller in DC microgrid systems," *IEEE Access*, vol. 12, pp. 140310–140328, 2024, doi: 10.1109/ACCESS.2024.3469815.

[38] V. Repecho, J. M. Olm, R. Grino, A. Doria-Cerezo, and E. Fossas, "Modelling and nonlinear control of a magnetically coupled multiport DC–DC converter for automotive applications," *IEEE Access*, vol. 9, pp. 63345–63355, 2021, doi: 10.1109/ACCESS.2021.3074696.

[39] O. Garpinger, T. Hägglund, and K. J. Åström, "Performance and robustness trade-offs in PID control," *J. Process Control*, vol. 24, no. 5, pp. 568–577, May 2014, doi: 10.1016/j.jprocont.2014.02.020.

[40] V. Mummadi and A. R. Bhimavarapu, "Robust multi-variable controller design for two-input two-output fourth-order DC–DC converter," *Electr. Power Compon. Syst.*, vol. 48, nos. 1–2, pp. 86–104, Jan. 2020, doi: 10.1080/15325008.2020.1736213.

[41] M. Rasouli, M. Mehrasa, A. Ganjavi, M. S. Sadabadi, H. Ghoreishy, and A. Ale Ahmad, "Lyapunov-based control strategy for a single-input dual-output three-level DC/DC converter," *IEEE Trans. Ind. Electron.*, vol. 70, no. 10, pp. 10486–10495, Oct. 2023, doi: 10.1109/TIE.2022.3217610.

[42] M. Veerachary and A. Trivedi, "Linear matrix inequality-based multivariable controller design for boost cascaded charge-pump-based double-input DC–DC converter," *IEEE Trans. Ind. Appl.*, vol. 58, no. 6, pp. 7515–7528, Nov. 2022, doi: 10.1109/TIA.2022.3201173.

[43] S. Sigurd, *NoMultivariable Feedback Control: Analysis and Design*, 2nd ed., Hoboken, NJ, USA: Wiley, 2005.

[44] K. Zhou and J. C. Doyle, *Essentials of Robust Control*, 1st ed., Upper Saddle River, NJ, USA: Prentice-Hall, 1996.

[45] J. Freudenberg and D. Looze, "Right half plane poles and zeros and design tradeoffs in feedback systems," *IEEE Trans. Autom. Control*, vol. AC-30, no. 6, pp. 555–565, Jun. 1985, doi: 10.1109/TAC.1985.1104004.

[46] K. Havre and S. Skogestad, "Effect of RHP zeros and poles on the sensitivity functions in multivariable systems," *J. Process Control*, vol. 8, no. 3, pp. 155–164, Jan. 1998, doi: 10.1016/s0959-1524(97)00045-0.

SHAHRIAR FARAJDADIAN (Member, IEEE) received the B.S. and M.Sc. degrees in electrical power systems engineering from Azad University, South Tehran Branch, Tehran, Iran, in 2012 and 2018, respectively. He is currently pursuing the Ph.D. degree in power electronics and control with the Department of Energy, Aalborg University, Denmark. In 2024, he was a Visiting Researcher with the DCE&S Group, Delft University of Technology. His research interests include power electronic converters, control systems, and the integration of renewable energy into the grid.

AMIN HAJIZADEH (Senior Member, IEEE) received the M.S. (Hons.) and Ph.D. (Hons.) degrees in electrical engineering from the K. N. Toosi University of Technology, Tehran, Iran, in 2005 and 2010, respectively.

From 2014 to 2016, he was a Postdoctoral Fellow with the Norwegian University of Science and Technology (NTNU), Trondheim, Norway. Since 2016, he has been an Associate Professor with the Department of Energy, Aalborg University, Denmark. He serves as the Project Manager for several industrial projects. His research interests include the control of distributed energy resources, power electronic converters for microgrids, and offshore power systems. He is an active member of the scientific program committees of multiple IEEE conferences. Additionally, he is a reviewer for several IEEE and IET journals and has served as a guest and an associate editor for special issues in IEEE, IET, and Elsevier journals.

MOHSEN SOLTANI (Senior Member, IEEE) received the M.Sc. degree in electrical engineering from the Sharif University of Technology, Tehran, Iran, in 2004, and the Ph.D. degree in electrical and electronic engineering from Aalborg University, Aalborg, Denmark, in 2008. He joined Eindhoven University of Technology, Eindhoven, The Netherlands, as a Visiting Researcher, in 2007. He fulfilled a Postdoctoral and an Assistant Professor Program with Aalborg University, Esbjerg, Denmark, from 2008 to 2012. In 2010, he joined Stanford University, Stanford, CA, USA. Since 2012, he has been an Associate Professor with the Department of Energy Technology, Aalborg University. In 2015, he completed a Research Leadership Training Program with the Harvard Business School, Boston, MA, USA. His current research interests include modeling, control, optimization, estimation, and fault detection and their applications to electromechanical and energy conversion systems, wind turbines, and wind farms.

PAVOL BAUER (Senior Member, IEEE) received the master's degree in electrical engineering from the Technical University of Kosice, Kosice, Slovakia, in 1985, and the Ph.D. degree from Delft University of Technology, Delft, The Netherlands, in 1995. He is currently a Full Professor with the Department of Electrical Sustainable Energy, Delft University of Technology, where he is also the Head of the DC Systems, Energy Conversion, and Storage Group. From 2002 to 2003, he worked partially at KEMA (DNV GL), Arnhem, The Netherlands, on different projects related to power electronics applications in power systems. He is also an Honorary Professor with the Politehnica University Timisoara, Timisoara, Romania. He has worked on many projects for industry concerning wind and wave energy, and power electronic applications for power systems, such as Smarttrafo, and HVdc systems, projects for smart cities, such as PV charging of electric vehicles, PV and storage integration, and contactless charging. He participated in several Leonardo da Vinci, H2020, and Electric Mobility Europe EU projects as a Project Partner (ELINA, INETELE, E-Pragmatic, Micact, Trolly 2.0, and OSCD) and a Coordinator (PEMCWebLab.com-Edipe, SustEner, and Eranet DCMICRO). He has published more than 95 journal articles and 350 conference papers in his field (with an H factor of 39 from Google Scholar and 29 from Web of Science). He is the author or co-author of eight books. He has organized several tutorials at international conferences. He holds nine international patents. He is also a member of the Executive Committee of the European Power Electronics Association (EPE) and international steering committees at numerous conferences. He received the title Prof. from the President of Czech Republic at the Brno University of Technology, Brno University of Technology, Brno, Czechia, in 2008, and Delft University of Technology, in 2016. He is also the Former Chairperson of the Benelux IEEE Joint Industry Applications Society, Power Electronics and Power Engineering Society Chapter, and the Chairperson of the Power Electronics and Motion Control (PEMC) Council.

HANI VAHEDI (Senior Member, IEEE) received the Ph.D. degree (Hons.) from École de Technologie Supérieure (ÉTS), University of Quebec, Montreal, Canada, in 2016. He received the Best Ph.D. Thesis Award from ETS, from 2016 to 2017. He has published more than 100 technical papers in IEEE conferences and Transactions. He also published a book on Springer Nature and a book chapter in Elsevier. He is the inventor of the PUC5 converter, holds multiple US/world patents, and transferred that technology to the industry, where he developed the first bidirectional electric vehicle dc charger based on his invention. After seven years of experience in industry as a power electronics designer and chief scientific officer, he joined Delft University of Technology (TU Delft), where he is currently an Assistant Professor at the DCE&S Group, working towards the electrification of industrial processes for clean energy transition. He is also leading the 24/7 Energy Hub project at The Green Village of TU Delft, implementing a local microgrid with renewable energy resources, green hydrogen production, and energy storage systems as the future of the clean energy transition. His research interests include multilevel converter topologies, control and modulation techniques, and their applications in the electrification of industrial processes and clean energy transition, such as smart grids, renewable energy conversion, electric vehicle chargers, green hydrogen production (electrolyzers), and fuel-cell systems. He was the Co-Chair of the IEEE Industrial Electronics Society (IES) Student and Young Professionals (S&YP) Committee and is serving as the IES Chapters Coordinator. He has been co-organizing special sessions and SYP forums at IEEE international conferences. He is also the Associate Editor for IEEE Transactions on Industrial Electronics, Open Journal of Industrial Electronics, and Open Journal of Power Electronics.